Detecting Small Moving Targets in Infrared Imagery

Adam Cuellar
University of Central Florida

DETECTING SMALL MOVING TARGETS IN INFRARED IMAGERY

by

ADAM THOMAS CUELLAR
B.S. University of Central Florida, 2019

A thesis submitted in partial fulfillment of the requirements
for the degree of Master of Science
in the Department of Electrical and Computer Engineering
in the College of Engineering & Computer Science
at the University of Central Florida
Orlando, Florida

Fall Term
2020

Major Professor: Abhijit Mahalanobis

ABSTRACT

Deep convolutional neural networks have achieved remarkable results for detecting large and medium sized objects in images. However, the ability to detect small objects has yet to achieve the same level performance. Our focus is on applications that require the accurate detection and localization of small *moving* objects that are distant from the sensor. We first examine the ability of several state-of-the-art object detection networks (YOLOv3 and Mask R-CNN [1] [2]) to find small moving targets in infrared imagery using a publicly released dataset by the US Army Night Vision and Electronic Sensors Directorate. We then introduce a novel Moving Target Indicator Network (MTINet) and repurpose a hyperspectral imagery anomaly detection algorithm, the Reed-Xiaoli detector [3], for detecting small moving targets. We analyze the robustness and applicability of these methods by introducing simulated sensor movement to the data. Compared with other state-of-the-art methods, MTINet and the ARX algorithm achieve a higher probability of detection at lower false alarm rates. Specifically, the combination of the algorithms results in a probability of detection of approximately 70% at a low false alarm rate of 0.1, which is about 50% greater than that of YOLOv3 and 65% greater than Mask R-CNN.

ACKNOWLEDGEMENTS

I would like to extend my sincere and heartfelt gratitude to my advisor Professor Abhijit Mahalanobis for the continuous support of my Masters research and his immense knowledge and experience in computer vision. His guidance has helped me gain a true understanding of computer vision applied to real world scenarios.

I would also like to thank my fellow colleagues at Lockheed Martin, William McDowell and Nicholas Shorter, for directing my knowledge of deep learning and its application in computer vision. Both have encouraged me to continue learning and have offered me opportunities to practice my knowledge on novel datasets.

TABLE OF CONTENTS

LIST OF FIGURES vi
LIST OF TABLES vii
LIST OF ACRONYMS viii
CHAPTER ONE: INTRODUCTION 1
  NVESD Dataset 2
  Literature Review 4
    YOLOv3 4
    Mask R-CNN 6
    ResNeSt 8
    Reed-Xiaoli Detector 9
    Convolutional Neural Network Improvements 10
CHAPTER TWO: PRELIMINARY EXPERIMENTS 14
  Dataset Partitioning 14
    Frame-by-Frame 15
    Difference Images 16
    Grouped Frames 17
  YOLOv3 Results 18
    Frame-by-Frame 18
    Difference Images 19
  YOLOv3-LSTM Results 21
  Mask R-CNN Results 22
    Frame-by-Frame 22
    Difference Images 23
  Experiment Analysis 24
CHAPTER THREE: METHODOLOGY 28
  MTINet 28
  MTINet-DW 35
  Combining MTINet and the Reed-Xiaoli Algorithm 37

Modeling Sensor Movement 38
CHAPTER FOUR: RESULTS 40
Evaluation of MTINet-1 using MSE and TCR loss functions 40
Evaluation of MTINet-2 and MTINet-CC 42
Evaluation of MTINet-CC with Simulated Sensor Movement 44
Performance Evaluation of MTINet-DW 46
Evaluation of the ARX Algorithm 48
Combining MTINet and the ARX Algorithm 49
CHAPTER FIVE: CONCLUSION AND FUTURE WORK 51
REFERENCES 54

LIST OF FIGURES

Figure 1: Example NVESD frames at day and night with targets at different ranges 3
Figure 2: Spatial Pyramid Pooling block 6
Figure 3: Convolutional Block Attention Module 11
Figure 4: Histogram of Pixels on Target in training and testing set 15
Figure 5: Example of bi-directional image differencing 16
Figure 6: Example of five frame blocks and the registration of two frames 17
Figure 7: YOLOv3 frame-by-frame training and testing set results 19
Figure 8: YOLOv3 difference images training and testing set results 20
Figure 9: YOLOv3-LSTM frame-by-frame training and testing set results 21
Figure 10: Mask R-CNN frame-by-frame training and testing set results 23
Figure 11: Mask R-CNN difference images training and testing set results 24
Figure 12: Activation Maps of trained feature extractors Darknet53 and ResNeSt50 ... 26
Figure 13: Predictions made by YOLOv3 and Mask R-CNN on successive frames 27
Figure 14: Example of ideal mask 29
Figure 15: Diagram of MTINet-1 32
Figure 16: Diagram of MTINet-2 33
Figure 17: Implementation of modified SPP module in MTINet-CC 35
Figure 18: Modified Convolutional Block Attention Module with a pointwise convolution 37
Figure 19: Example of simulated sensor movement 39
Figure 20: MTINet 1 results on NVESD testing set with MSE loss 41
Figure 21: MTINet 1 results on NVESD testing set with the modified TCR loss 42
Figure 22: MTINet 2 results on NVESD testing set 42
Figure 23: MTINet-CC results on NVESD testing set 43
Figure 24: MTINet-CC results on NVESD testing set with misaligned frames 44
Figure 25: MTINet-CC results on NVESD testing set with registered frames 45
Figure 26: MTINet-CC results on NVESD testing set with and without sensor movement 46
Figure 27: MTINet-DW results on NVESD testing data with registered frames 47
Figure 28: Activation Map of trained MTINet-DW 48
Figure 29: ARX Algorithm results on NVESD testing data with registered frames 49
Figure 30: Combined MTINet-DW and ARX algorithm results on the NVESD testing data with registered frames 50
Figure 31: Comparison of MTINet-DW, the ARX algorithm, and their combination on the NVESD testing set 50
Figure 32: Comparison of results given simulated sensor movement 53

LIST OF TABLES

Table 1: Comparison of object detection networks on the MS COCO dataset [1] [2] [7] [8] for small, medium, and large objects 2
Table 2: Preliminary experiment results at IOU of 0.5 and score threshold of 0.5 25
Table 3: Comparing results of highest performance experiments 52

LIST OF ACRONYMS

AP	Average Precision
CBAM	Convolutional Block Attention Module
CNN	Convolutional Neural Network
FAR	False Alarm Rates
FOV	Field of View
IOU	Intersection over Union
LSTM	Long Short-Term Memory
mAP	Mean Average Precision
MS COCO	Microsoft Common Objects in Context
MSE	Mean Squared Error
MTINet	Moving Target Indicator Network
MWIR	Mid-Wave Infrared
NVESD	Night Vision and Electronic Sensors Directorate
PCA	Principal Component Analysis
PDet	Probability of Detection
POT	Pixels on Target
R-CNN	Region-based Convolutional Neural Network
ROC	Receiver Operating Characteristic
RoI	Region of Interest
RPN	Region Proposal Network
SE	Squeeze-And-Excitation
SOTA	State-of-the-art
SPP	Spatial Pyramid Pooling
SURF	Speeded Up Robust Features
TCR	Target to Clutter Ratio
YOLO	You Only Look Once

CHAPTER ONE: INTRODUCTION

High performance, deep convolutional neural network (CNN) based object detectors have been largely developed for use with RGB data. There are many popular methods for detecting and localizing objects from images; however, the detection performance for small objects remains a challenging problem.

Modern CNN's are benchmarked on common datasets such as ImageNet [4] and Microsoft common objects in context (MS COCO) [5]. Each of these datasets contains natural images with discernible features and relatively large objects. MS COCO defines small, medium, and large objects as those with *areas* (defined in terms of total pixels) of area $< 32^2$, $32^2 <$ area $< 96^2$, and area $> 96^2$ respectively. Current state-of-the-art (SOTA) networks, such as You Only Look Once (YOLO) and Mask R-CNN, perform inadequately on the small objects in the COCO dataset. [6]

As shown in Table 1, the performance of detectors on medium and large objects significantly surpasses their performance on small objects. The average precision (AP) on large objects is more than twice of that on small objects for each of these networks. Therefore, we ask the question: What improvements can be made to increase the performance of small object detection techniques, and can it be realized on types of imagery other than RGB data?

Table 1: Comparison of object detection networks on the MS COCO dataset [1] [2] [7] [8] for small, medium, and large objects

Network	AP	AP_S	AP_M	AP_L
YOLOv3	33.0%	**18.3%**	35.4%	41.9%
Mask R-CNN	**37.1%**	16.9%	**39.9%**	**53.5%**

First, we aim to tackle this problem by repurposing existing object detection algorithms for find small moving targets, and systematically evaluating their performance on infra-red imagery. Specifically, we train and evaluate these algorithms using a publicly released dataset by the US Army Night Vision and Electronic Sensors Directorate (NVESD). Both YOLOv3 and Mask R-CNN perform poorly on this dataset with less than a 20% mean average precision (mAP). This provides the motivation for developing novel custom CNN networks, and for re-examining other statistical methods such as the Reed-Xiaoli detector (which is widely used for hyperspectral anomaly detection) for detecting small moving targets in infra-red imagery.

NVESD Dataset

The data set provided for this research is a collection of mid-wave infrared (MWIR) imagery collected by the US Army Night Vision and Electronic Sensors Directorate [6]. The data includes vehicular targets moving at a constant velocity along a circle with a diameter of about 100 meters. This movement allows us to obtain all azimuth angles of the vehicles. The data was collected at day and night, at different ranges, and contains ten different types of vehicles. These vehicles belong to both military and civilian classes including BTR70, BMP, BRDM, T62, T72, ZSU23, 2S3, MTLB, SUV, and Pickup truck. Ground truth information was provided which contained information about the target's location, range, and class. The vehicles can be anywhere between 1000 to 5000 meters in range. Other information is also provided; however, we do not directly use this data. Figure 1 below shows the diversity between the day and night infrared photos as well as the relative size of the target within the image.

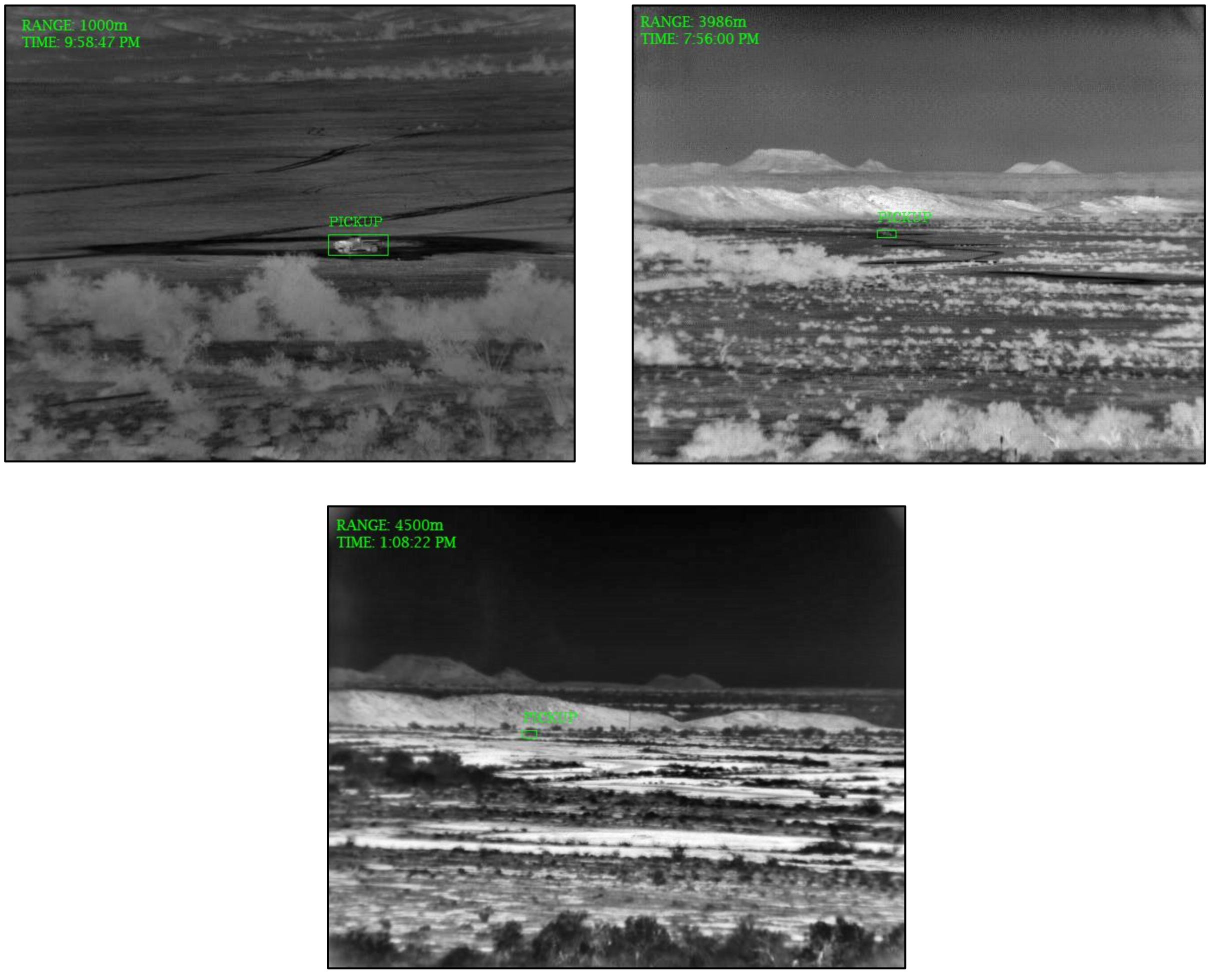

Figure 1: Example NVESD frames at day and night with targets at different ranges

Literature Review

Modern object detection models are generally built in two different ways, two-stage object detectors and one-stage object detectors. Both types of detectors have a backbone that is used to extract features and encode data for the head of the network. For a two-stage network, the head predicts the coordinates of an object and then classifies that object. For a one-stage network, the head predicts both the coordinates and the classification of an object simultaneously. One-stage networks are often much faster but often less accurate [1]. Therefore, we assess the use of each as a benchmark for the performance of target detection in the NVESD dataset.

YOLOv3

You Only Look Once is a one stage object detection network developed by Joseph Redmon and Ali Farhadi. The performance of YOLO has improved across different versions such as YOLO, YOLOv2, YOLOv3 tiny, and YOLOv3. As most object detection networks, YOLOv3 consists of a feature extractor as well as three separate detection heads. The feature extractor, Darknet53, is made up of 53 convolutional layers and outperforms larger models such as Resnet-101 on the ImageNet dataset for classification [1]. Prediction is done at three different scales using each of the detection heads. Each head is responsible for reducing the image into a grid of different sizes. Specifically, the three heads reduce the image into $\left(\frac{h}{2^5}, \frac{w}{2^5}\right)$, $\left(\frac{h}{2^4}, \frac{w}{2^4}\right)$, and $\left(\frac{h}{2^3}, \frac{w}{2^3}\right)$ where h and w are the height and width of the input image. Each cell in the grid is responsible for predicting an object if the object's center falls within that cell. The output of each head is a 3D tensor encoding bounding box coordinates, the *objectness* of the detections, and class predictions. The bounding box coordinates output by the detection head are an offset from the top left corner of the image added to a proportion of the bounding box priors. The bounding box priors, or anchors, are computed using k-means clustering on all bounding boxes found in the training set.

The original loss functions for YOLOv3 is composed of the mean squared error (MSE) of the bounding box coordinates, the binary cross entropy of the objectness score, and the binary cross entropy of the multi-class predictions of each bounding box. This loss function since has been improved by removing the MSE of the bounding box coordinates and substituting the intersection over union (IOU) loss. The intersection over union is the area of intersection between the predicted bounding box and its respective ground truth divided by the area of union.

Zhanchao Huang and Jianlin Wang first introduced the Spatial Pyramid Pooling (SPP) block to YOLO using YOLOv2 [9]. The addition of this block increased the mean average precision of YOLOv2 on the PASCAL VOC2007 test dataset by approximately 2%; therefore, the idea was applied to YOLOv3 as well [9]. The SPP block consists of three max-pooling layers, each with different kernel sizes. Initially the block contained the kernel sizes 5x5, 7x7, and 13x13; however, when adding the block to YOLOv3 the 7x7 kernel was replaced with a 9x9 kernel. The addition of this module emphasizes high frequency features within the image thus increasing the networks ability to detect and classify an object. Figure 2 shows the implementation of the SPP module.

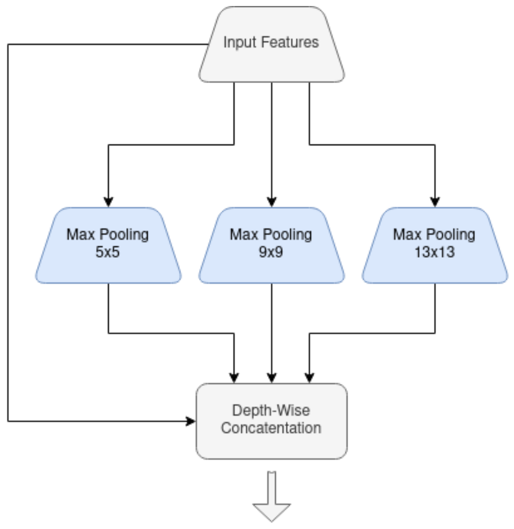

Figure 2: Spatial Pyramid Pooling block

Mask R-CNN

Mask Region-based CNN (R-CNN) is a two-stage detector developed by He et al. Mask R-CNN is an extension of Faster R-CNN which adds a branch for predicting an object mask in parallel with the existing bounding box prediction branch. Similar to Faster R-CNN, the network consists of a region proposal network (RPN) and a classification stage. The addition of the object mask prediction occurs in the classification stage where the network is responsible for predicting the class and box offsets. This branch allows for the output of a binary mask for each region of interest (RoI).

In addition to the new branch, Mask R-CNN appends the mask loss L_{mask} to Faster R-CNN's loss function. This multi-task loss function is defined as $L = L_{cls} + L_{box} + L_{mask}$. The classification loss (L_{cls}) and bounding-box loss (L_{box}) are consistent with Faster R-CNN; however, the mask loss is defined as the average binary cross-entropy loss [2]. This definition extends the network's ability to generate masks for each class. The dedicated mask branch removes any competition between classes, decoupling the mask and class prediction.

Unlike Faster R-CNN, Mask R-CNN uses RoIAlign in place of RoIPool. RoIPool is the standard operation for extracting a feature map from each region of interest. This layer takes a RoI, defined as the top-left corner and height and width (*x, y, h, w)*, and divides the *h* × *w* window into an *H* × *W* grid of sub-windows, where *H* and *W* represent the spatial-extent of the layer. Each sub-window is approximately $\frac{h}{H} \times \frac{w}{W}$ and the features of the sub-window are aggregated to the corresponding output grid cell using max pooling. This process introduces misalignments and therefore reduces the accuracy of pixel-level masks. To prevent this, RoIPool is replaced with RoIAlign which removes the quantization of features and accurately aligns them with the input image. This is done using bilinear interpolation to calculate the exact values of the features at regularly sampled locations in each bin which are then aggregated using a max or average pool [2].

ResNeSt

He et al. developed Mask R-CNN using two different backbones. Both of these feature extractors are variants of ResNet named ResNet-101-FPN and ResNeXt-101-FPN. Since the development of Mask R-CNN, other variations of ResNet have been created and have surpassed prior implementations performance on the ImageNet classification task. More specifically, ResNeSt, introduced by Zhang et al. has surpassed the performance of both ResNet-101 and ResNeXt-101 in both image classification and as an object detection backbone. On ImageNet, ResNeSt-101 achieves an 81.97% top-1 accuracy whereas ResNet-101 and ResNeXt-101 achieve a 77.37% and 78.89% top-1 accuracy, respectively. On MS COCO, using Faster-RCNN, a ResNeSt-101 backbone achieves a 44.72% mean average precision while ResNet-101 and ResNeXt-101 backbones achieve a 37.3% and 40.1% mean average precision, respectively. The success of ResNeSt can be attributed to the unique cross-channel representations within the networks architecture [10].

Inspired by the Squeeze-and-Excitation (SE) network, ResNeXt, and other similar methods, ResNeSt generalizes the channel-wise attention into feature-map group representation [10]. This is done using a Split-Attention block which allows for attention across different feature-map groups using grouped convolutions. The Split-Attention block applies a grouped convolution to split the input feature into K groups. The split feature-map group is referred to as *cardinal groups.* The cardinal groups can be split further using the *radix* hyperparameter, R, resulting in $G = KR$ groups. Within the cardinal groups, a combined representation is obtained by element-wise summation across the splits. After the summation, global contextual information can be obtained using global average pooling across spatial dimensions, s^k, which is then collected using channel-wise soft attention. Channel-wise soft attention is defined in equation (1) below where *c* denotes the *c*-th channel and *G* determines the weight of each split *i.*

$$A_i^k(c) = \begin{cases} \dfrac{\exp\left(G_i^c(s^k)\right)}{\sum_{j=0}^{R} \exp\left(G_i^c(s^k)\right)}, & if\ R > 1 \\ \dfrac{1}{1 + \exp\left(-G_i^c(s^k)\right)}, & if\ R = 1 \end{cases} \tag{1}$$

The cardinal groups are then concatenated channel-wise and used for a shortcut connection if the input and output feature-maps are of the same shape [10].

Reed-Xiaoli Detector

Developed by Reed and Yu, the Reed-Xialoli algorithm is a constant False Alarm Rate detector used to detect anomalous pixels in hyperspectral data. The algorithm assumes the clutter of an image follows a Gaussian distribution and uses the Gaussian Log-likelihood Ratio Test to identify anomalies that have a low likelihood. More specifically, given a hyperspectral image of depth *D,* the algorithm implements a filter by equation (2):

$$RX(x_i) = (x_i - \mu)^T K_{DxD}^{-1} (x_i - \mu) \tag{2}$$

where x is a $D \times 1$ column pixel vector from the matrix, μ is the global sample mean, and K is the sample covariance matrix of the image. This form of the equation is also known as the Mahalanobis distance [11].

The Reed-Xiaoli algorithm is essentially the reverse operation of principal component analysis (PCA). PCA is known for being able to decorrelate matrix data while preserving information about the image in separate components that represent a different part of uncorrelated data. Therefore, PCA has been used to compress image information into major components which are individuated by the eigenvector of K that correspond to large eigenvalues. However, it was not designed to be used for detection or classification. Although, it can be assumed that if the image contains data which occur with low probabilities, such as the size of the target samples being small, then the minor components of K that occur with small eigenvalues would contain information about this data. Consequently, the Reed-Xiaoli algorithm can capitalize on this property and use this to detect anomalous pixels.

Convolutional Neural Network Improvements

Convolutional Neural Networks can be constructed in many ways, and new architectural components are often incorporated to increase performance. These components are often modular and can be applied to other architectures for similar increases in performance. Therefore, we explore several state-of-the-art neural network modules that have helped significantly increase performance in image classification and object detection models.

Convolutional Block Attention Module

The significance of attention in neural network architectures has been widely studied in recent literature and is used to guide the network where to focus [12]. Attention allows the network to increase the representation of important features. Attention can be applied to the channels of an input feature as well as spatially. The Convolutional Block Attention Module (CBAM) applies attention to both to emphasize the meaningful features across the spatial and channel dimensions. This is done by applying a channel attention block and spatial attention block sequentially. Figure 3 below shows an overview of the CBAM implementation. Woo et al. reported that the implementation of CBAM in ResNet and ResNeXt improves the performance of the networks and decreases both the top-1 and top-5 percent error on the ImageNet classification task.

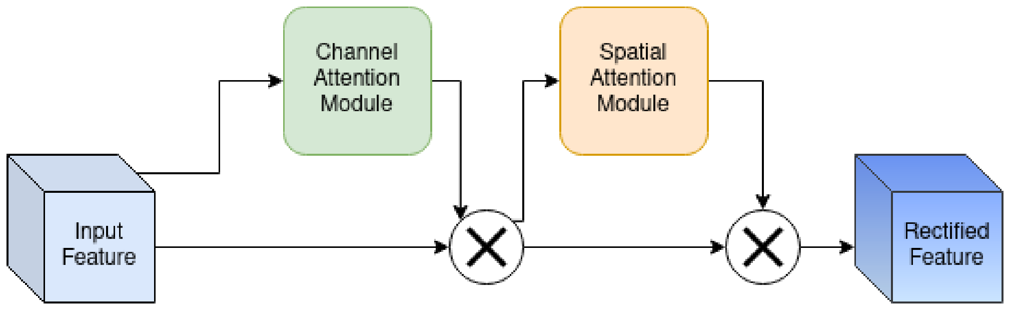

Figure 3: Convolutional Block Attention Module

The channel attention module is similar to the Squeeze-and-Excitation block implemented by Hu et al. [13]. The SE block attempts to represent channel-wise dependencies using global average pooling; however, Woo et al. use both average and max pooling to highlight distinct features for a finer channel-wise excitation. The global max and average pooling layers generate descriptive spatial information which is then passed into a multi-layer perceptron with one hidden layer. The output features are summed, elementwise, and passed to a sigmoid layer prior to being multiplied to the input feature channels.

The spatial attention module focuses on the inter-spatial relationship between features to help the network emphasize the features related to the object of interest. To compute this, average and max pooling are applied across the channel axis, and the results are concatenated depth-wise. The concatenated feature maps are convolved using a standard convolution which then produces the spatial attention map. The sigmoid function is applied to the spatial attention map and the output of the channel attention module is multiplied by this.

Grouped Convolutions

Grouped convolutions, also known as sub-separable convolutions, consist of splitting the channels of an input feature into non-overlapping segments. These segments, or groups, are convolved with the desired number of filters independently and the results are concatenated along the channel axis. This separation can significantly reduce the parameter count of a model as well as increase the performance [14]. For a regular convolution, the number of parameters can be calculated by $p = k * c^2$, where k represents the size of the kernel and c represents the number of filters. For a grouped convolution, the number of parameters is calculated by $p = k * \frac{c^2}{g} + c^2$, where g is the number of groups.

CHAPTER TWO: PRELIMINARY EXPERIMENTS

We assess the performance of current state-of-the-art networks such as YOLOv3 and Mask R-CNN on the NVESD dataset. Each network was trained on the frame-by-frame data configuration and on the difference images. The principal performance metric are the probability of detection and the false alarm rates defined as:

$$PDet = \frac{number\ of\ detected\ targets}{number\ of\ total\ targets} \tag{3}$$

$$FAR = \frac{number\ of\ false\ detections}{total\ number\ of\ total\ frames} \tag{4}$$

For the following experiments, we consider a target as detected if the IOU between the predicted bounding box and the ground truth bounding box is greater than or equal to 50%.

Dataset Partitioning

The dataset was split into a training and testing set using the provided range information. To focus on the ability to detect small objects, we use the targets at ranges 4000 to 4500 meters for training and any farther ranges for testing. Therefore, 10484 images were used with 7090 images allocated for training and 3394 images for testing. Figure 4 shows the distribution of the number of Pixels on Target (POT) for the training and testing sets. The Pixels on Target is the number of pixels within the ground truth bounding box. Looking at Figure 4 we can see that the training set accurately represents the testing set in terms of POT. We also note that the maximum area meets the criteria of a small object with the area < 32^2, as defined in MS COCO.

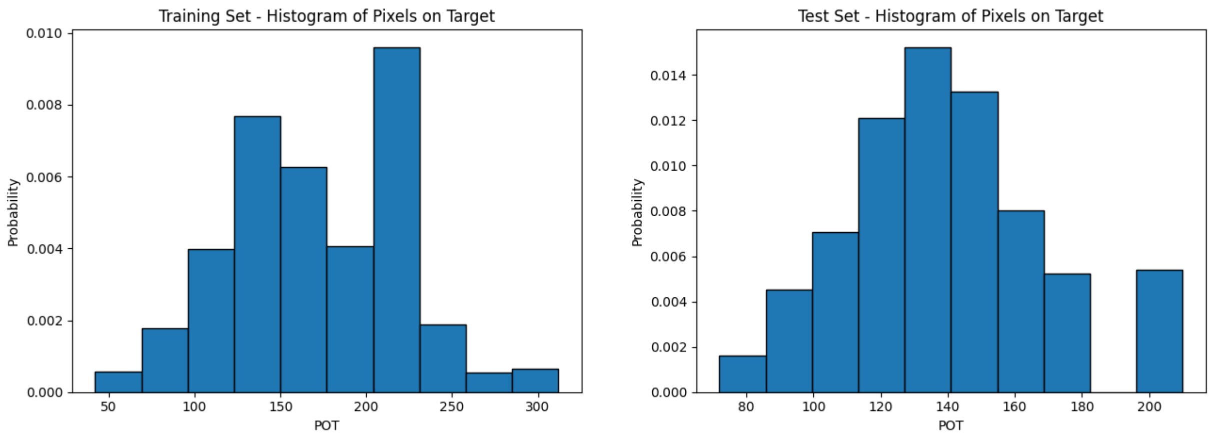

Figure 4: Histogram of Pixels on Target in training and testing set

Throughout our experiments, we used the split dataset in different ways. More specifically, focused on finding targets using i) a single frame, ii) using the difference images, and iii) using groups of consecutive frames. A detailed description of each of these configurations is provided below.

Frame-by-Frame

To examine the innate ability of the algorithms to detect small objects, we used the data by feeding it one frame at a time. This limited the network to using only spatial and contextual information for detecting and localizing an object, but no temporal or motion information is used.

Difference Images

In order to exploit temporal information to find objects, we use bi-directional frame differencing. To compute the difference images, we take the magnitude of the difference between an image with four other frames. More specifically, let x_i represent the $i-th$ image in a sequence of consecutive frames from a 30Hz video stream. Using images that are five frame apart (i.e. x_{i-10}, x_{i-5}, x_i, x_{i+5} and x_{i+10}) , we compute the four *difference images* $|x_{i-10}-x_i|$, $|x_{i-5}-x_i|$, $|x_{i+5}-x_i|$, and $|x_{i+10}-x_i|$. Figure 5 below shows an example of using bi-directional differencing to obtain the input to our algorithms.

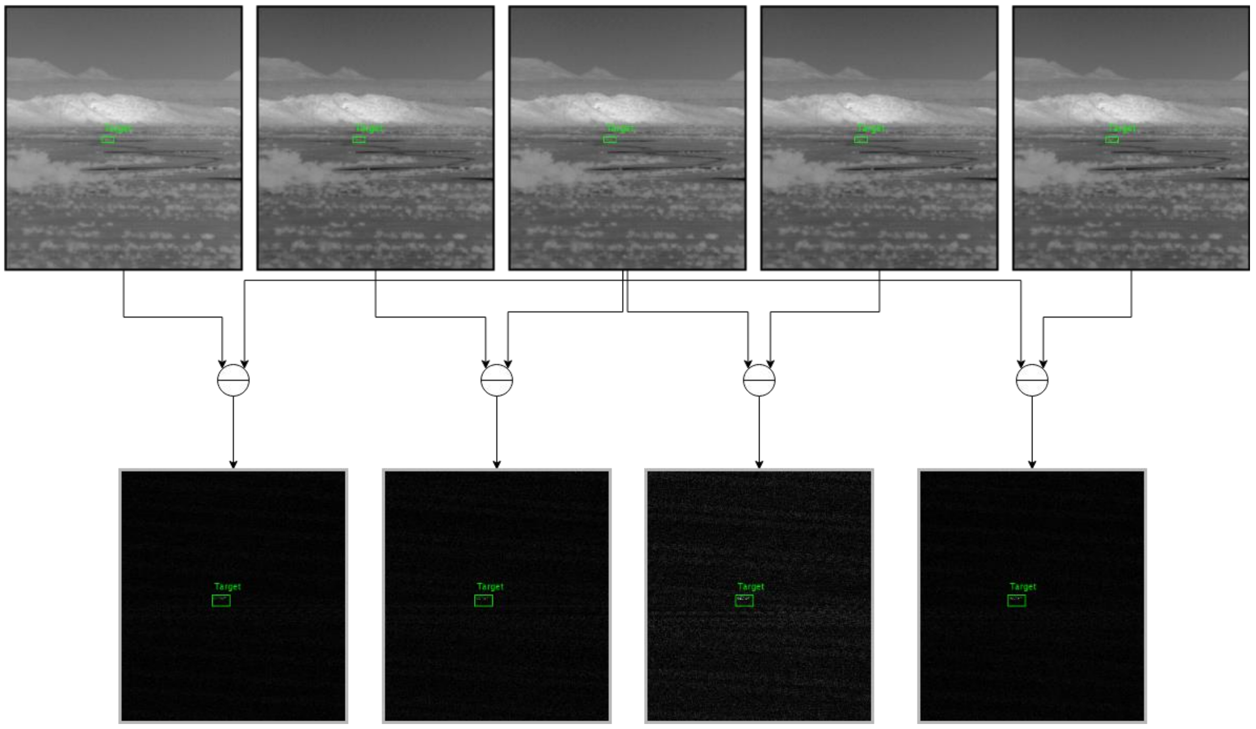

Figure 5: Example of bi-directional image differencing

Grouped Frames

Frame differencing can be directly used for finding moving targets; however, this requires the frames to be accurately registered to one another or captured by a stable sensor. In practical application, sensor stability is not guaranteed, and registration errors can occur. Therefore, to exploit temporal information without relying on perfect registration, we feed the data as a block of stacked frames (e.g. a block with the five frames x_{i-10}, x_{i-5}, x_i, x_{i+5}, and x_{i+10}) directly to the algorithm. Intensity-based image registration can be still used to roughly align the block of frames with respect to the middle image, mainly to remove any large sensor movement. Figure 6 shows an example of this where a block of frames is registered using speeded up robust features (SURF) [15].

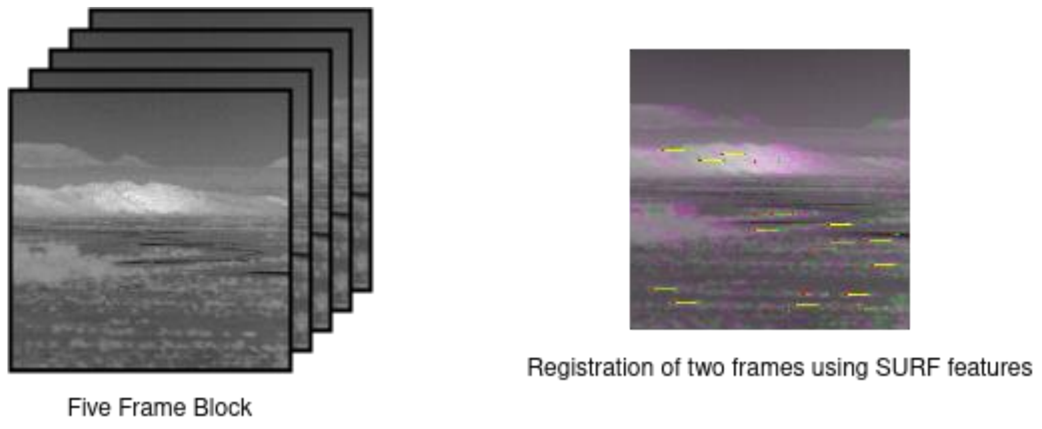

Figure 6: Example of five frame blocks and the registration of two frames

YOLOv3 Results

We trained YOLOv3 on the NVESD dataset and received the following results on the training and testing sets. Specifically, we initialize YOLOv3 with pretrained weights from the MS COCO dataset and train on the NVESD dataset until the training loss no longer decreases.

Frame-by-Frame

Using the frame-by-frame configuration, YOLOv3 achieves a mean average precision of approximately 95.87% on the training set; however, the mean average precision on the testing set is just 3.52%. Figure 7 below contains the probability of detection vs false alarm rate receiver operating characteristic (ROC) curves for both the training and testing set on the frame-by-frame data. For the training set, the probability of detection is greater than 90% but when evaluating the testing set, we see a maximum probability of detection of approximately 7%.

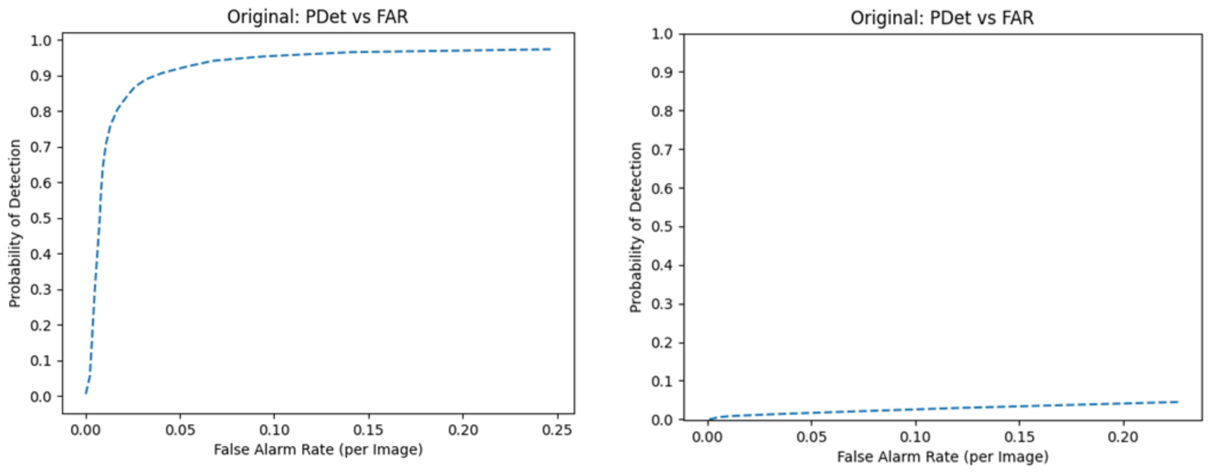

Figure 7: YOLOv3 frame-by-frame training and testing set results

The underwhelming results of YOLOv3 on the testing set indicates the model may have overfit to the training data; therefore, we assessed the results of the network every 1000 iterations. After reviewing the probability of detection and false alarm rate at each of those iterations, we assume the network is unable to efficiently generalize to the testing set due to the highly cluttered environments. In order to combat this, we attempt to lessen the background clutter and aid the network in exploiting spatiotemporal information by modifying the input to be the difference images between frames.

Difference Images

Using the difference images, YOLOv3 achieves a mean average precision of 96.36% and 20.68% on the training and testing sets, respectively. Figure 8 below shows the probability of detection vs false alarm rate ROC curves for both the training and testing set on the difference images data. The results on the training set show the network maintained its ability to learn the localization of a target with the probability of detection remaining above 90% while the false alarm rate drops from 25% to 8%. The probability of detection improved for the testing set as well, increasing by approximately 23%.

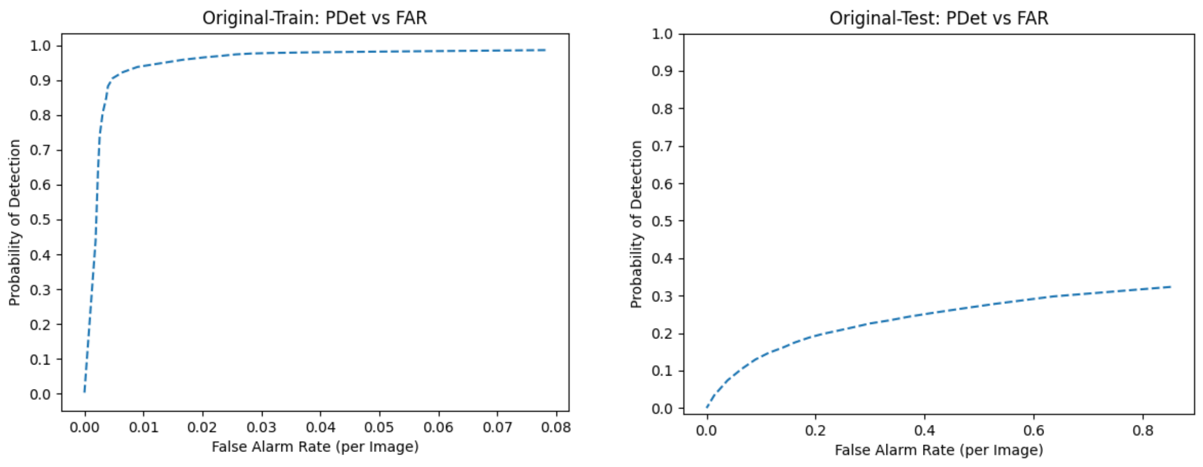

Figure 8: YOLOv3 difference images training and testing set results

The increase in detection ability is also associated with an increase in false alarms. The maximum false alarm rate increased by almost 60%, suggesting that the network cannot differentiate between the effects of background subtraction and apparent target motion in the difference images. Therefore, we implement a modification of the YOLOv3 network by including Long Short-Term Memory (LSTM) [16] layers to assist the network in learning the temporal information between frames. More specifically, the convolutional layer before each branch leading to the detection heads is replaced with a convolutional LSTM layer.

YOLOv3-LSTM Results

The goal of including convolutional LSTM layers is to allow the network to exploit temporal information across successive frames; therefore, we only train and test on the frame-by-frame data configuration. Unlike the grouped frames, the model is fed each frame individually and the LSTM layer is responsible for learning the dependencies between each frame. On the training set, the model achieves a 94.80% mean average precision with a maximum probability of detection of 97.20%. Although this is a slight drop in performance, there is also a slight increase in performance on the testing set with a 4.48% mean average precision and 10% maximum probability of detection. Compared to the previous experiment with YOLOv3, the false alarm rate increased significantly for both the training and testing sets with a 10% and 40% increase, respectively. Figure 9 below shows the ROC curves on the training and testing sets of the frame-by-frame configuration.

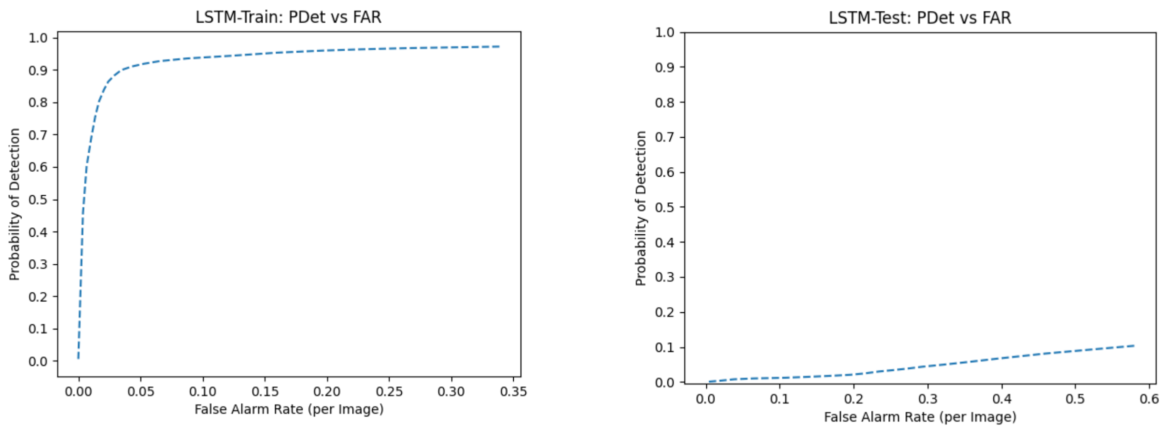

Figure 9: YOLOv3-LSTM frame-by-frame training and testing set results

Mask R-CNN Results

We trained Mask R-CNN, with ResNeSt as the backbone, on the NVESD dataset and observed the following results on the training and testing sets. Specifically, we initialize Mask R-CNN with pretrained weights from the MS COCO dataset and train on the NVESD dataset until the training loss no longer decreases. We chose ResNeSt due to its state-of-the-art attention mechanism.

Frame-by-Frame

On the frame-by-frame data, Mask R-CNN achieves a mean average precision of 93.67% and 1.34% on the training and testing set, respectively. On the training set, Mask R-CNN accurately detects targets with a maximum probability of detection of 90%; however, the false alarm rate is significantly higher than the results of YOLOv3. Figure 10 below shows the performance of Mask R-CNN on the training and testing sets.

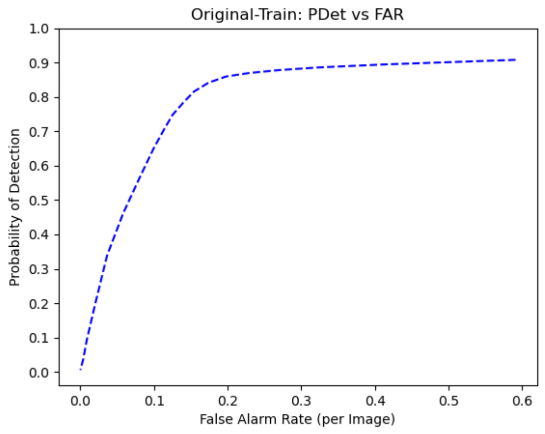

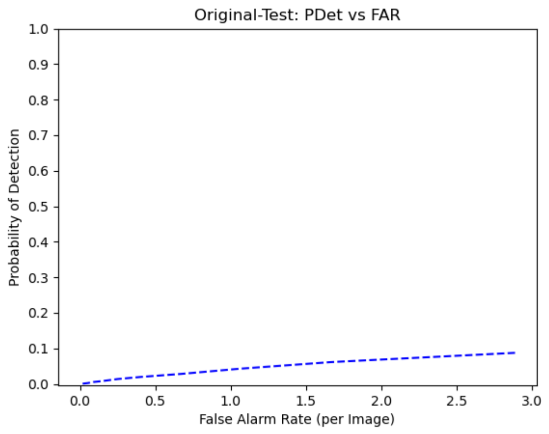

Figure 10: Mask R-CNN frame-by-frame training and testing set results

Mask R-CNN also fails to detect most targets in the testing set using single frames, therefore reinforcing the notion of the inability of these networks to generalize properly given highly cluttered environments.

Difference Images

Similar to YOLOv3, Mask R-CNN performs slightly better on the difference images compared to the frame-by-frame testing set. However, the performance on the training set drops with a mean average precision of 87.36% and a max probability of detection of approximately 78%. Figure 11 below shows the results of Mask R-CNN on the training and testing sets. For the testing set, the difference images produced a similar probability of detection while also decreasing the false alarm rate to 1.75 false alarms per image.

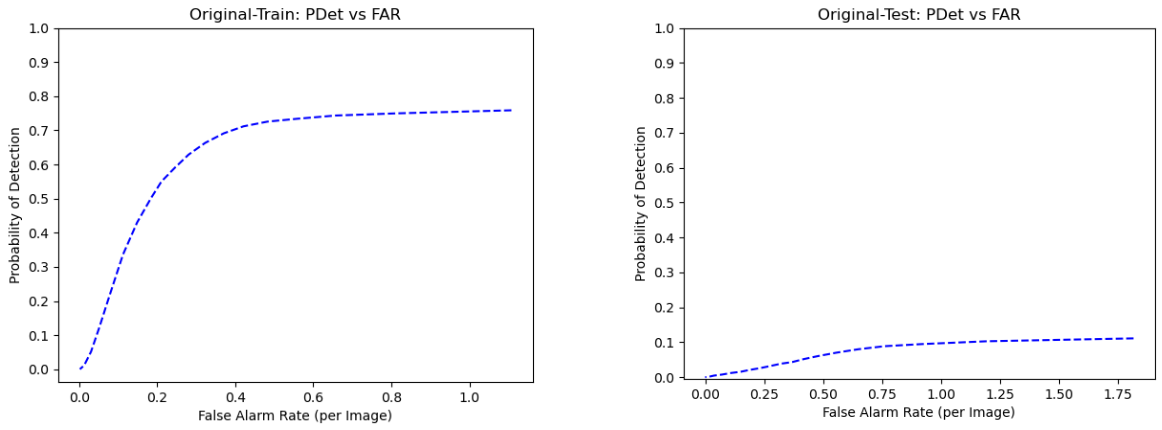

Figure 11: Mask R-CNN difference images training and testing set results

Experiment Analysis

Detecting small targets in the NVESD dataset poses a challenge to current state-of-the-art networks. Both YOLOv3 and Mask-RCNN fail to accurately detect targets in the testing set despite the effort to reduce the complexity of the problem. As seen in Table 2 below, the most optimal results were obtained using YOLOv3 with the difference images as an input. This configuration provided the highest probability of detection on the testing set at a confidence threshold of 50% but also produced the most false alarms per frame. Due to the nature of this data and the potential application of these detectors in real-time systems, this level of performance is inadequate and conveys a potential shortcoming of the state-of-the-art networks. To develop a deeper understanding of what these limitations may be, we analyze the trained networks further.

Table 2: Preliminary experiment results at IOU of 0.5 and score threshold of 0.5

Network	Data Configuration	Training			Testing		
		mAP (%)	*PDet (%)*	*FAR (%)*	*mAP (%)*	*PDet (%)*	*FAR (%)*
YOLOv3	Frame-by-Frame	95.87	80.57	1.71	3.52	0.44	**0.46**
	Difference Images	**96.36**	**94.77**	**1.28**	**20.68**	**20.64**	24.07
YOLOv3-LSTM	Frame-by-Frame	94.80	91.04	4.31	4.48	2.44	21.53
Mask R-CNN	Frame-by-Frame	93.67	74.76	12.51	1.34	0.15	3.19
	Difference Images	87.36	59.02	24.51	3.96	3.84	31.98

Both YOLOv3 and Mask R-CNN were able to adapt to the training set but failed to generalize enough to accurately detect targets in the testing set. We assume this is due to the combination of small targets in an extremely cluttered environment. To further investigate this, we use guided backpropagation on the feature extractors of each of the networks. With guided backpropagation, we are able to produce a localization map of regions in each image that are significant to the network [17]. This localization map is overlayed on the original test set images to provide the heatmaps seen below. Figure 12 below contains a heatmap produced on the same image by both YOLOv3's feature extractor, Darknet53, and Mask R-CNN's feature extractor, ResNeSt50.

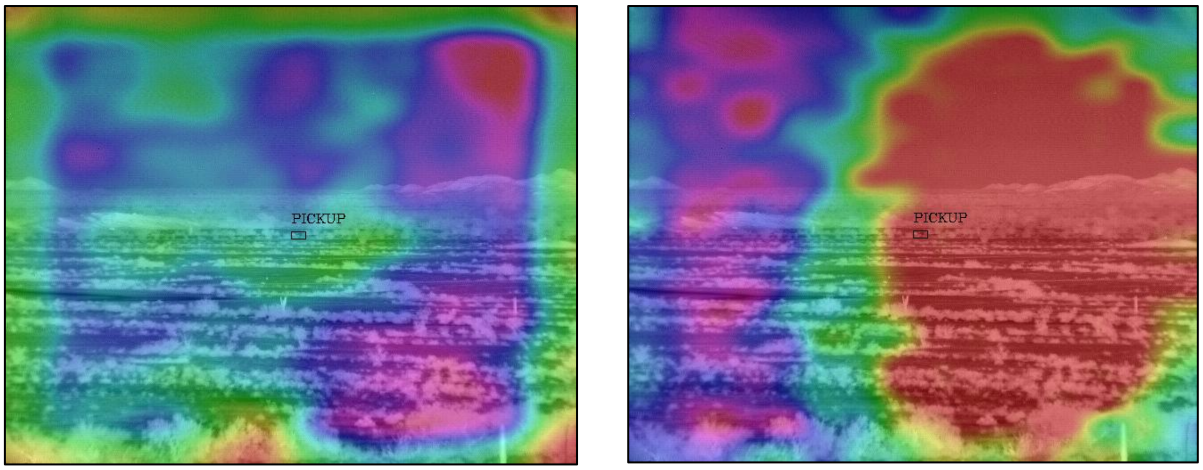

Figure 12: Activation Maps of trained feature extractors Darknet53 and ResNeSt50

The heatmap produced by Darknet53 shows the network has difficulty highlighting features of the target and instead seems to be misled by the dense vegetation present in this image. Conversely, ResNeSt50 produces a heatmap with clear localization of the area around the target; however, these activations are not specific to the target itself. To see how the localization of high activations effects the detection predictions, we visualize all detections made on this same scene with a confidence score greater than 5%. Figure 13 below contains predictions by YOLOv3 and Mask R-CNN made on two successive frames. Both frames come from the same sequence and were taken ten seconds apart. The green bounding box corresponds to the ground truth, the red corresponds to YOLOv3's predictions, and blue corresponds to Mask R-CNN's predictions. To accurately analyze the individual ability of each network, non-max suppression was omitted.

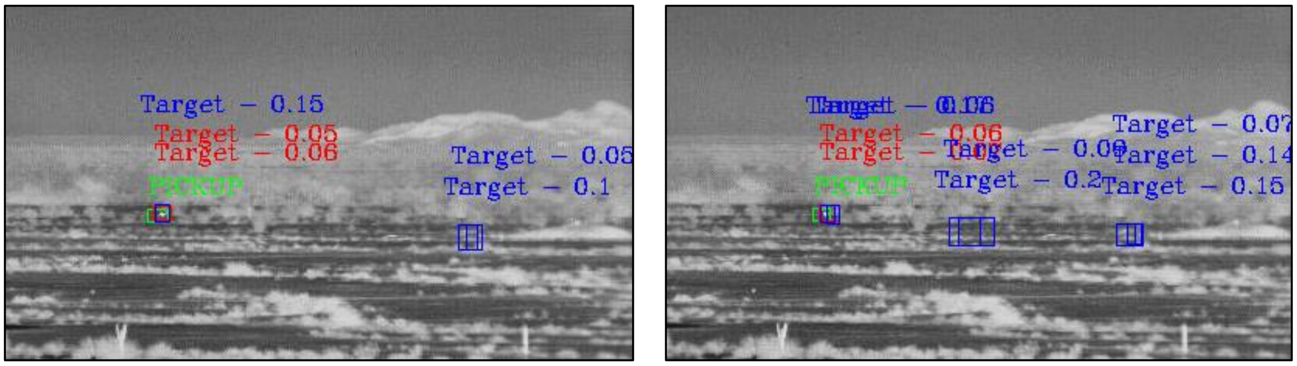

Figure 13: Predictions made by YOLOv3 and Mask R-CNN on successive frames

For these specific frames, both networks were able to accurately predict the location of the target. In both instances, YOLOv3 made accurate predictions but with very low confidence scores. On the other hand, Mask R-CNN made mostly inaccurate predictions with a negligible difference in confidence scores. Mask R-CNN's false positives can most likely be attributed to the high activations on the right of the heatmap shown in Figure 12. Although the frames were taken ten seconds apart, there is only a difference of three pixels in the targets position on the x-axis. The inconsistency between Mask R-CNN's predictions across the two frames and YOLOv3's low confidence scores indicate the inability of the networks to discern target versus clutter. Therefore, it is reasonable to conclude that the networks are unable to generalize properly and are confused by the cluttered environment.

CHAPTER THREE: METHODOLOGY

After analyzing the results of the preliminary experiments, we propose a new CNN architecture dubbed as Moving Target Indicator Network (or MTINet) that exploits temporal information along with spatial anomaly to find small moving targets in highly cluttered data. We also compare the performance of the MTINet to a statistical anomaly detection algorithm known as the Reed Xiaoli detector and combine the two to help boost performance at very low false rates. We refer to the Reed-Xiaoli anomaly detection as the ARX algorithm.

MTINet

For the development of the Moving Target Indicator network (MTINet) we aim to increase the probability of detection while keeping the false alarm rate low. Specifically, our goal is to increase the detection rate at very low false alarm rates between 0 to 0.5 false alarms per frame. Following the same methodology described in Grouped Frames, we seek to simultaneously exploit spatial and temporal information by processing a group of five image frames.

To properly utilize a group of five frames as the input to each of our networks, we define the ground truth in a manner similar to those of semantic segmentation tasks [18]. For our purposes, the location of the center of the object is most significant. Therefore, we create the ideal *desired response* (required for training the networks) by first producing a mask with value of “1” at the center of each target (but zero everywhere else), and then convolve the mask with a gaussian kernel to provide a smooth shape for the ideal response. Figure 14 shows an example of a mask created for a frame from the NVESD dataset.

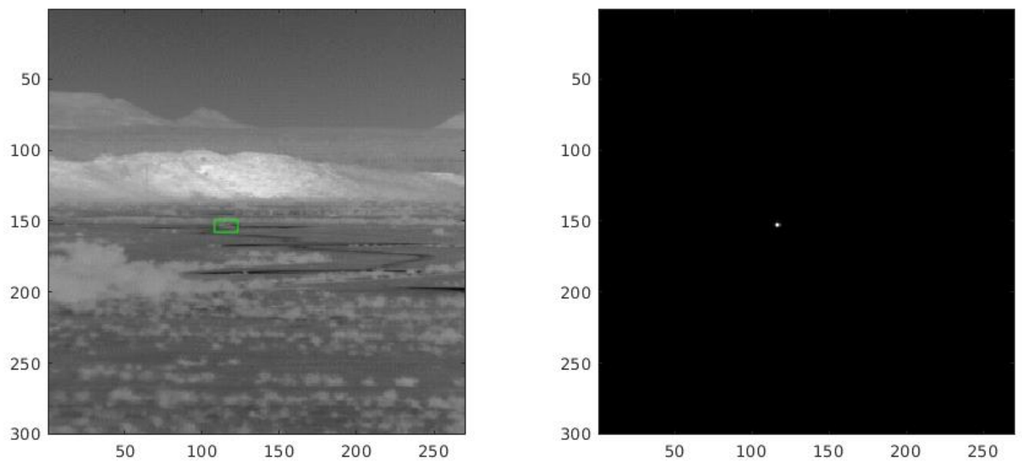

Figure 14: Example of ideal mask

Conventional regression-based training methods minimize the MSE loss between the actual and ideal desired response of the network. However, we observed that this approach does not work well for our application where the shape of the desired response is not important. Rather, it is essential to produce a strong response at the true location of the targets, while attenuating the output of the network produced in response to clutter. This is achieved by using the *Target to Clutter Ratio* (TCR) cost function developed by McIntosh et al [19]. The TCR cost function aims to maximize the response of the target while minimizing the response of clutter. This is done by minimizing the ratio in equation (5):

$$J_{TCR} = \frac{\frac{1}{N}\sum y_i^T y_i}{\sqrt[N]{\prod x_i^T x_i}} \qquad (5)$$

This is the ratio of the arithmetic mean of the energy of the clutter samples, y_i, to the geometric mean of the energy of the target samples x_i [19]. To minimize this ratio the numerator must be small while the denominator must be large. Therefore, the summation of the clutter response must be small thereby ensuring that the algorithms' response to clutter is minimized. Similarly, the algorithms' response to all targets must be large to ensure the product in the denominator of equation (5) is large. The minimization of this loss function causes the network to learn how to discriminate effectively between targets and clutter.

To increase the ability of generalization across different scenes, we use zero mean and unit variance normalization to normalize each block of frames going into the network. We also utilize batch normalization layers to ensure the stability of the gradients throughout the duration of training. The network takes into account each and every pixel by only using convolutions with a stride of one.

To properly exploit the spatial and temporal information of each frame the design of our networks must utilize features from each image in the block of frames. Therefore, each frame must be processed by the network independently. First, we implement this by passing the input to five separate routes. The first convolutional layer of each route extracts one of the five channels using frozen weights of all ones in the respective channel index of the kernel and zeros elsewhere. This allows each frame to be initially processed by a separate branch of the network (labeled 1 through 5 in Figure 15), and then the respective outputs to be combined for further processing by the stem of the network. We designate this configuration of the network as the first version of MTINet, i.e MTINet-1.

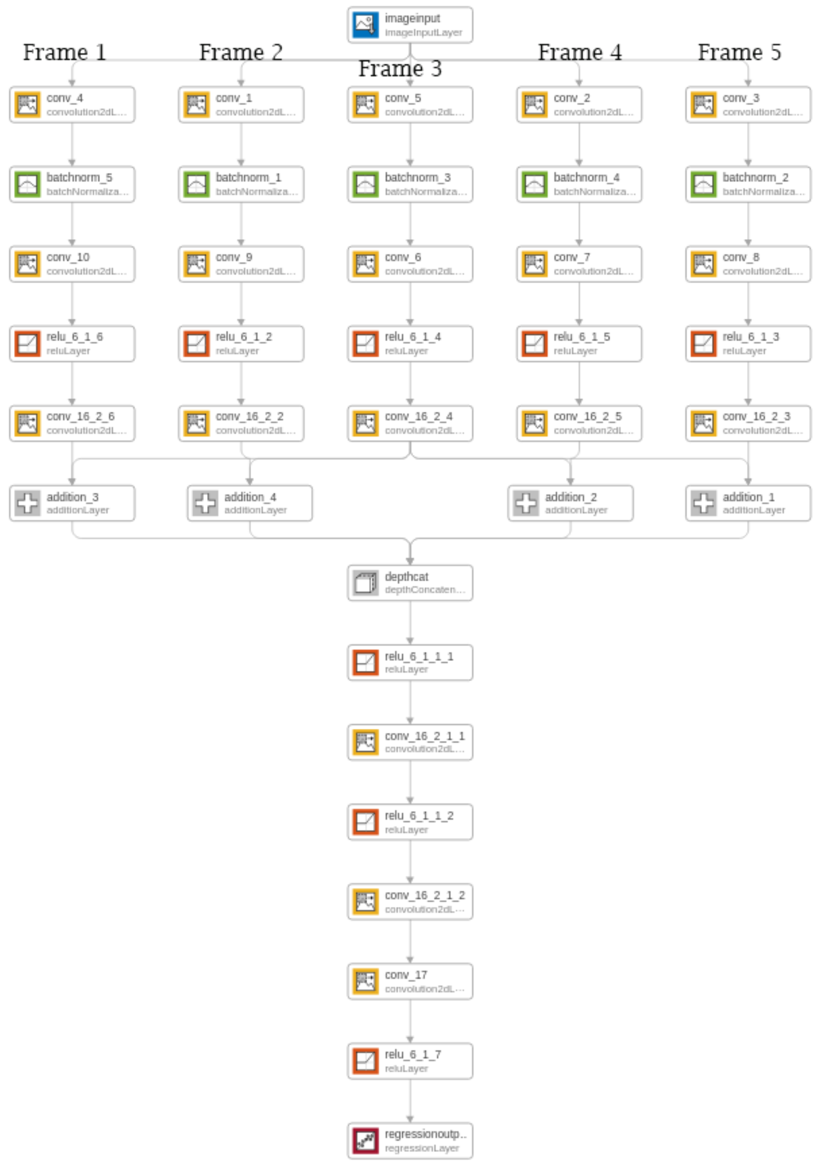

Figure 15: Diagram of MTINet-1

To extract each region of interest, we locate the coordinates and value of the maximum response from the output of the network. We replace all values in a $20 \, x \, 20$ window around the maximum response with value of the minimum response to ensure the detection is not counted more than once. We continue this process for up to ten regions of interest. The values extracted from the regions of interest are then normalized and used as the confidence score of the respective detection.

For moving platforms, frame differencing can introduce false alarm due to improper registration. To avoid this, MTINet must operate directly on the sequence of frames and learn the cross-dependencies between them; therefore MTINet-1 connects the five branches by summing their outputs, and depth-wise concatenating the results. Specifically, we add the output of the branch processing each frame, to the output of the middle branch. In other words, we concatenate the results of pair-wise addition between branch 3 and all other branches. Thereafter, the block of features is passed to the stem of the network where it is processed further using standard convolutions.

Although four connections between the branches provided favorable results, we sought to further improve the network by increasing the possible cross-dependencies between the frames the network. We achieved this in MTINet-2 by increasing the number of pairwise branch additions to twelve, as shown in Figure 16.

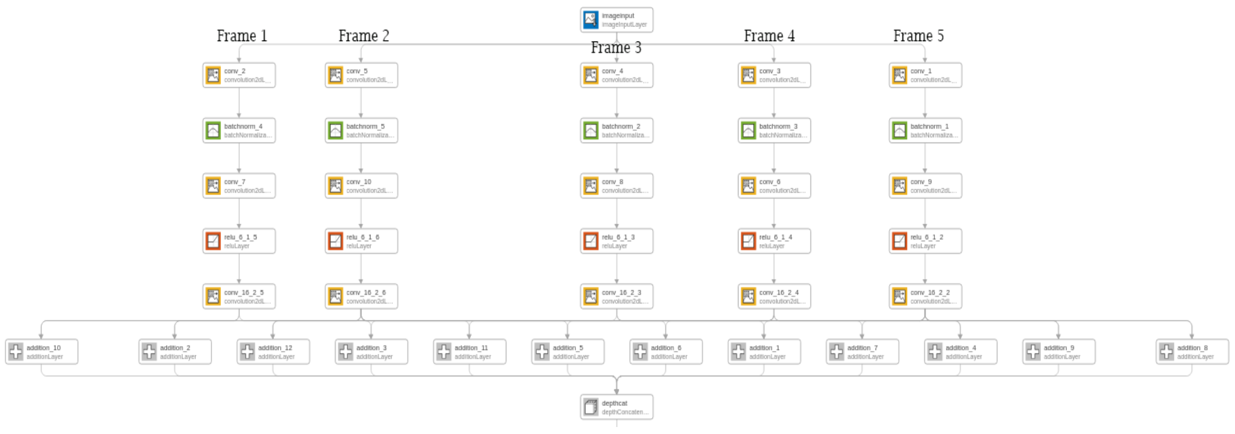

Figure 16: Diagram of MTINet-2

To further improve the performance of the MTINet, we introduce the Spatial Pyramid Pooling block which has shown a promising increase in performance in state-of-the-art detectors such as YOLOv3 [9]. The purpose of this block is to increase the range tolerance of the network as well as emphasizing high frequency features. We include this block into the stem of the network after the depth-wise concatenation of the cross-dependencies between frames. Unlike the original implementation, we use a convolutional layer, C_i, prior to the SPP module to process the features provided by the depth-wise concatenation layer and use the output of this convolution as the input to a pointwise convolution, C_p, prior to the max-pooling layers. Traditionally, the convolution prior to the max-pooling layers is used for depth-wise concatenation along with the results of the max-pooling. Instead of using C_p as the skip connection, we use C_i to guide the network into using C_p to emphasize single-pixel values related to the target prior to the max-pooling. C_i is then used for the depth-wise concatenation. Figure 17 below shows the modification of the Spatial Pyramid Pooling block for MTINet. We refer to this iteration of MTINet as MTINet-CC.

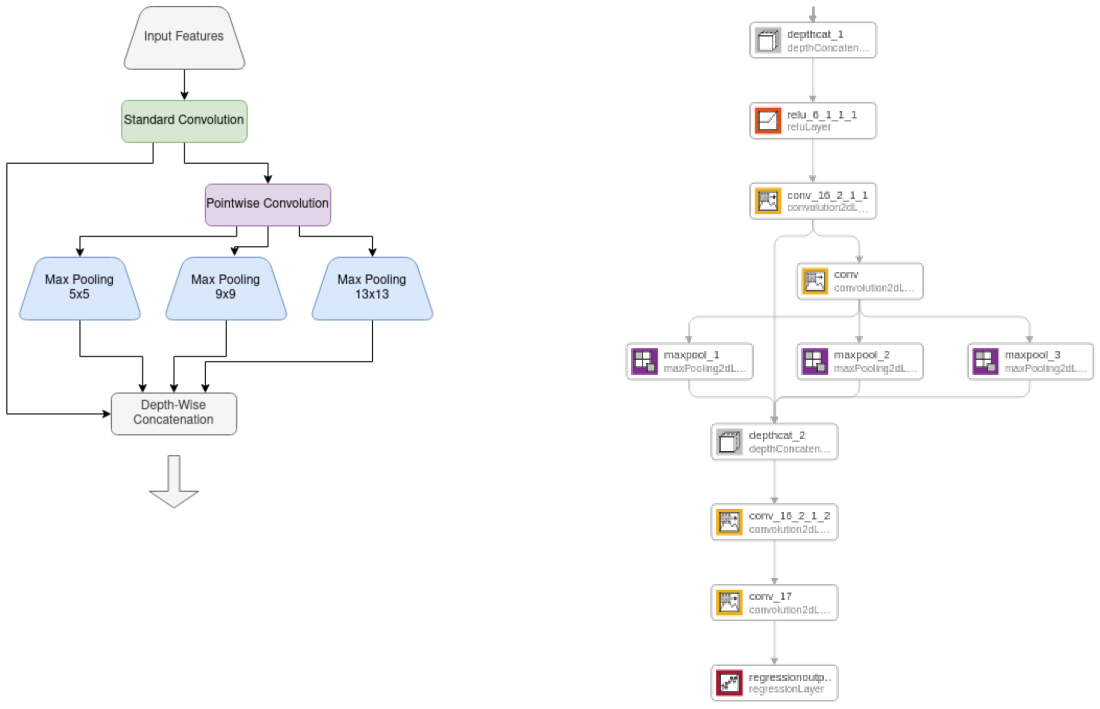

Figure 17: Implementation of modified SPP module in MTINet-CC

MTINet-DW

The final variant of the MTINet seeks to decrease the processing complexity introduced by the splitting of the block of frames into isolated streams as well as allow the network to emphasize cross-dependencies, as necessary. Explicit connections between frames through element-wise addition may limit the networks ability to learn the targets position through changes of the scene over time. Therefore, we replace the splitting of the input frame group with depth-wise convolutions and label this version as MTINet-DW.

As before, our goal is to maximize the performance of this network while keeping its depth and complexity similar to that of the original MTINet. Each stream of MTINet 1 and 2 had three convolutions - the first convolution is used to extract the appropriate frame whereas the other two convolutions are used for extracting the necessary features for the remainder of the network. The depth-wise convolutions mimic the processing occurring within each stream. With the removal of the multiple branches, we no longer need the first convolution. The depth-wise convolutions are then used to apply filters to each frame individually and to increase the amount of learned features from each frame independently.

We then utilize a derivative of the attention modules from the Convolutional Block Attention Module. To include the concept of attention without suppressing necessary features we modify the implementation to emphasize both the spatial and inter-channel relationship of features. This is done by using a structure similar to the spatial-attention module with a small change in the convolution operation following the max-pooling and average-pooling layers shown below in Figure 18. Similar to the spatial-attention module, we utilize the pooling layers to emphasize the spatial information from the extracted features provided by the depth-wise convolutions. However, unlike the Convolutional Block Attention Module implementation, we utilize a pointwise convolution on the depth-wise concatenated features extracted from the pooling operations. It is anticipated that the pointwise convolution allows for the combination of information, through the reduction of the number of filters, in a manner that accentuates the independent features of each frame, and thereby develops the necessary cross-dependencies between them. The output of this convolution is then passed into a sigmoid function prior to being multiplied with the original input features. Finally, the output of our attention module is then passed onto the stem of the network which remains similar to the second iteration of MTINet with the inclusion and matching placement of the SPP block.

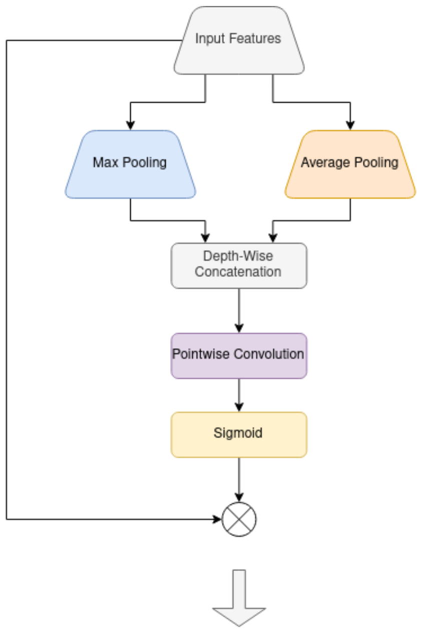

Figure 18: Modified Convolutional Block Attention Module with a pointwise convolution

Combining MTINet and the Reed-Xiaoli Algorithm

The Reed-Xiaoli algorithm was originally developed for detecting anomalies in hyperspectral data. This algorithm exploits the statistical properties of the data in the channel dimension and does not require any training. We repurpose the Reed Xiaoli detector to find moving targets in a stack of registered image frames. Our goal is to use this detector as a baseline for performance comparison, and also to ultimately combine the power of data driven learning techniques such as CNNs with the advantages of statistical detection techniques. As described in Reed-Xiaoli Detector, the quadratic distance computations can be easily implemented by reshaping the data cube into a 2D array where the global mean is subtracted resulting in matrix *M. M* is then divided by its covariance matrix resulting in matrix *R*. During initial experiments, we recognize the inverse of the covariance tends to become extremely large in certain instances. To avoid this, we calculate the Moore-Penrose Psuedoinverse of *M* to produce matrix *N.* We then multiply matrix *M* and matrix *N* resulting in matrix *P.* The Mahalanobis Distance is then calculated between matrix *P* and matrix *R.*

While both MTINet and the ARX algorithm can be used individually, we also evaluate a combination of the two methods that combines the benefits of each method. This is achieved by allowing each algorithm to make predictions given an input of a group of frames. Each algorithm returns a list of detections along with their confidence score. We then normalize each list independently and combine all predictions and use the range of confidence scores to separate likely detections versus false alarms.

Modeling Sensor Movement

Imaging systems for detection and surveillance often use panning sensors for covering a wide field of view. In such scenarios, the sensor moves horizontally in "step-stare" fashion, collecting images as it pans from left to right or vice versa. As a result, the background scenery in the individual frames appears to also shift position, and the stack of frames must be stabilized before the detection algorithms can be used. To examine the robustness of the algorithms when the image frames are shifted, we introduce simulated sensor movement to the NVESD dataset. To do so we use a 300×300 window from within the 512×640 image frame to mimic the sensor's field of view (FOV). The window is then shifted to the left and right using a saw-tooth waveform to mimic sensor movement. The window is moved 5 pixels for each frame for a maximum displacement of 50 pixels. We assume all pixels in the scene move equally when the sensor undergoes an angular rotation. Figure 19 below shows the sawtooth waveform used and the result of displacement on five consecutive frames. The small arrow in two of the images indicates an example of a background feature that appears shifted due to the simulated sensor movement. The shifted frames are then re-aligned (or stabilized) using image registration techniques with SURF features. In this case, frames one, two, four, and five are all registered to frame three and are then passed into the algorithms for processing.

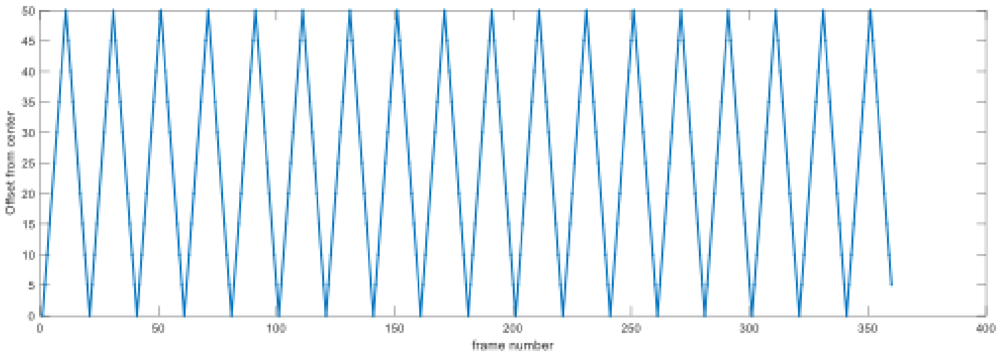

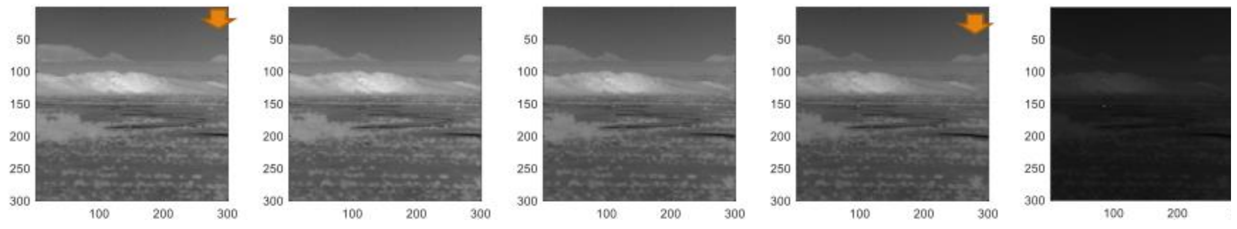

Figure 19: Example of simulated sensor movement

CHAPTER FOUR: RESULTS

We conduct experiments using each of the proposed networks, as well as the repurposed ARX algorithm, to evaluate their ability to find small moving targets in challenging background clutter. We compare ROC curves of Probability of Detection vs False Alarm Rate on the NVESD testing set to compare and contrast the performance of the proposed algorithm and its variants. The ROC curve shows the ability of the algorithm to accurately detect targets over varying thresholds. Generally, at higher false alarm rates we can detect more targets; however, we are mainly concerned with the detection ability at very low false alarm rates. Specifically, we focus on the ability to increase the probability of detection below 0.5 false alarms per frame. We first evaluate MTINet-1 with both the MSE and TCR loss functions. Based on the results, we choose to continue with the TCR loss function for optimizing other variants of MTINet. We then evaluate the performance of the remaining MTINet variants and then evaluate the ARX detector's performance. Finally, we evaluate the combination of both MTINet-DW and the ARX algorithm.

Evaluation of MTINet-1 using MSE and TCR loss functions

The ROC curves show below in Figure 20 represent the performance of MTINet-1 trained using the mean squared error loss function and four frame cross-dependencies. We observe that this network easily outperforms state of the art networks in detecting small moving targets for the NVESD testing set. Figure 20 below shows the results of MTINet-1 at both high and low false alarm rate ranges.

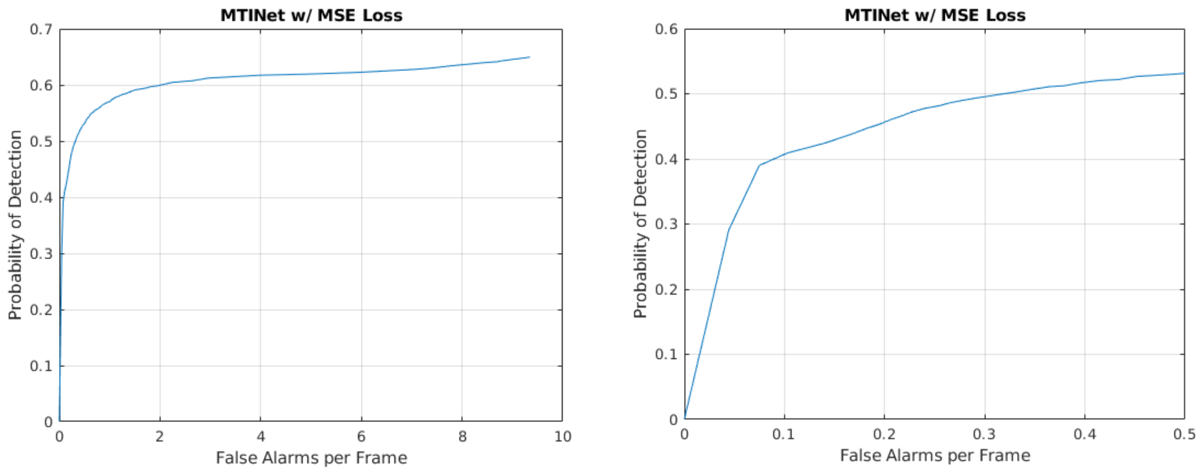

Figure 20: MTINet 1 results on NVESD testing set with MSE loss

The ROC curve on the right shows the detection performance at low false alarm rates between zero and 0.5 false alarms per frame. To further improve the probability of detection at low false alarm rates we change the loss function to the modified TCR cost function. With the same network, we are able to increase the results just by this change in loss function alone. At a false alarm rate of 0.5, the probability of detection using the MSE loss is approximately 53% while with the TCR loss it is 60%. At higher false alarm rates, more targets are found using the TCR loss. Specifically, at a false alarm rate of 5.0, with the TCR loss the probability of detection is 80% whereas with the MSE loss it is about 62%.

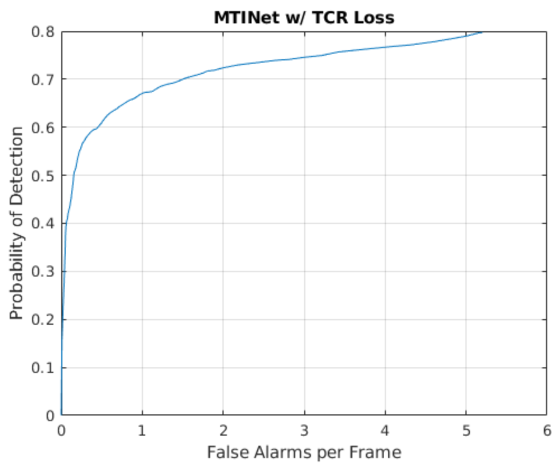

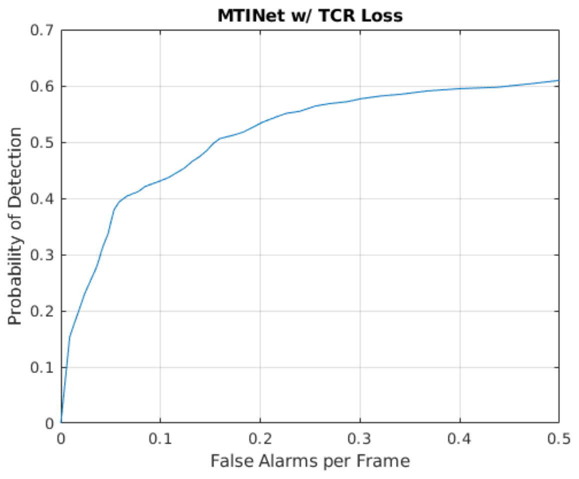

Figure 21: MTINet 1 results on NVESD testing set with the modified TCR loss

Evaluation of MTINet-2 and MTINet-CC

Since the TCR loss function yields better results than the MSE loss function, we use this to train and evaluate MTINet-2 and all the other variants. Recall that MTINet-2 uses twelve cross-dependencies rather than four for MTINet-1.

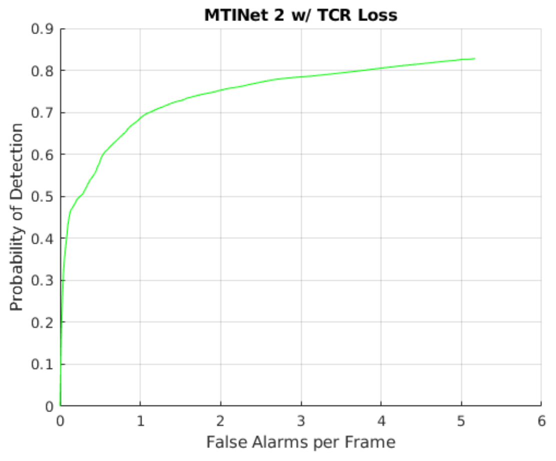

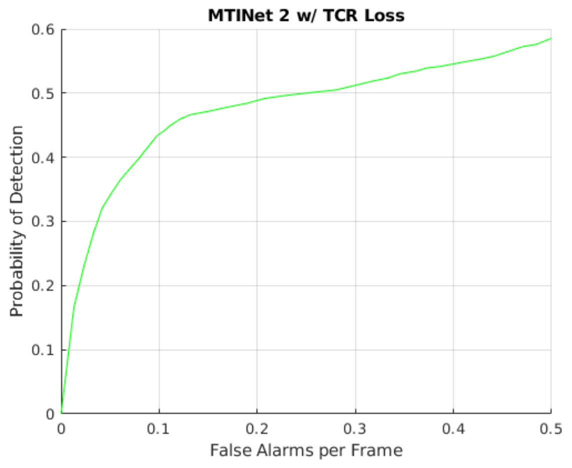

Figure 22: MTINet 2 results on NVESD testing set

Figure 22 shows that MTINet-2 increases the overall probability of detection. However, we also notice a slight decline in the lower false alarm ranges. Using MTINet 1 with the TCR cost function resulted in a probability of detection slightly above 60% at a false alarm rate of 0.5 false alarms per frame. At the same false alarm rate, MTINet 2 reached a probability of detection of slightly below 60%. Therefore, to improve the probability of detection at the left hand of the ROC curve, we augment MTINet 2 with the modified Spatial Pyramid Pooling (SPP) layer shown in Figure 17, and is now referred to as MTINet-CC. As shown in Figure 23 below, at a false alarm rate of 0.5 MTINet-CC notably outperforms our previous iterations with a probability of detection of approximately 83%. At the higher false alarm ranges, MTINet-CC can achieve a probability of detection of nearly 100%.

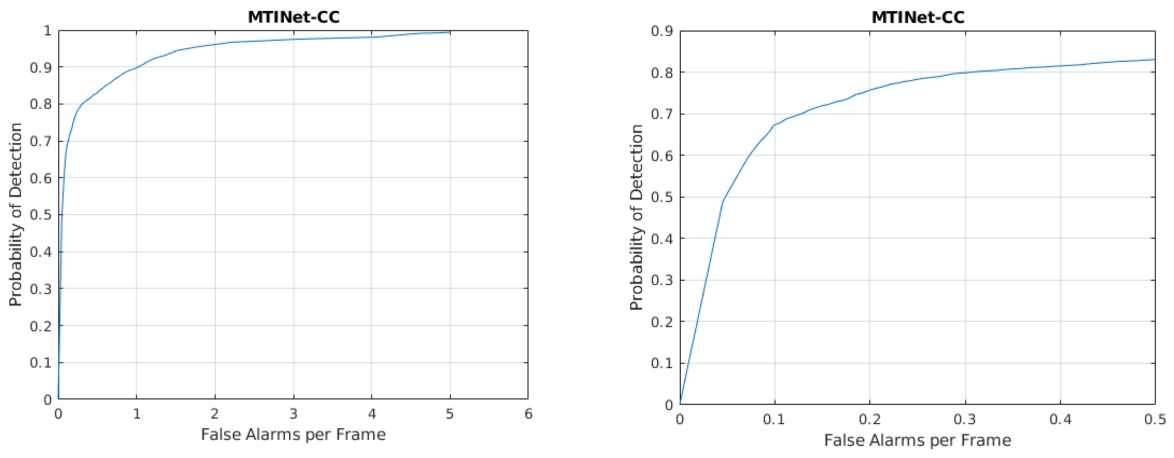

Figure 23: MTINet-CC results on NVESD testing set

Evaluation of MTINet-CC with Simulated Sensor Movement

We further examine the capabilities of MTINet-CC for detecting moving targets when the sensor is also horizontally panning across the scene. As described in Modeling Sensor Movement, we translate each frame approximately 5 pixels with a maximum displacement of 50 pixels and re-train and test the network on the group of misaligned images. Figure 24 below shows the results of introducing misalignment to the NVESD dataset on MTINet-CC.

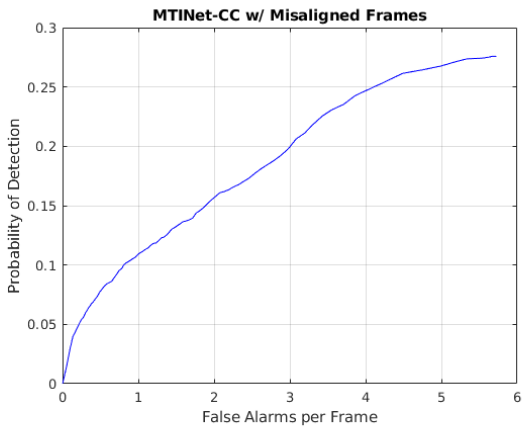

Figure 24: MTINet-CC results on NVESD testing set with misaligned frames

The results without any registration between frames is poor with a maximum probability of detection of approximately 27%. We believe the movement between the frames prevents the network from accurately learning the effect of target motion which gets confused by the movement of the background. It is possible that the network could be trained to learn the distinction between target versus background movement if substantially more training images were available. However, in the absence of large amounts of training data, we reduce the effects of misalignment by registering the group of frames to the middle frame using SURF features. The results of this registration are not perfect and introduces residual errors, both in background and in target signature. The network must learn to discriminate between the changes due to the targets' movement, and residual background errors, and generalize it to the test data. Implementing this process in a real-world system is realistic and can lessen the effects of major misalignment between frames. Figure 25 below shows the effect of registering the frames prior to passing them into the network.

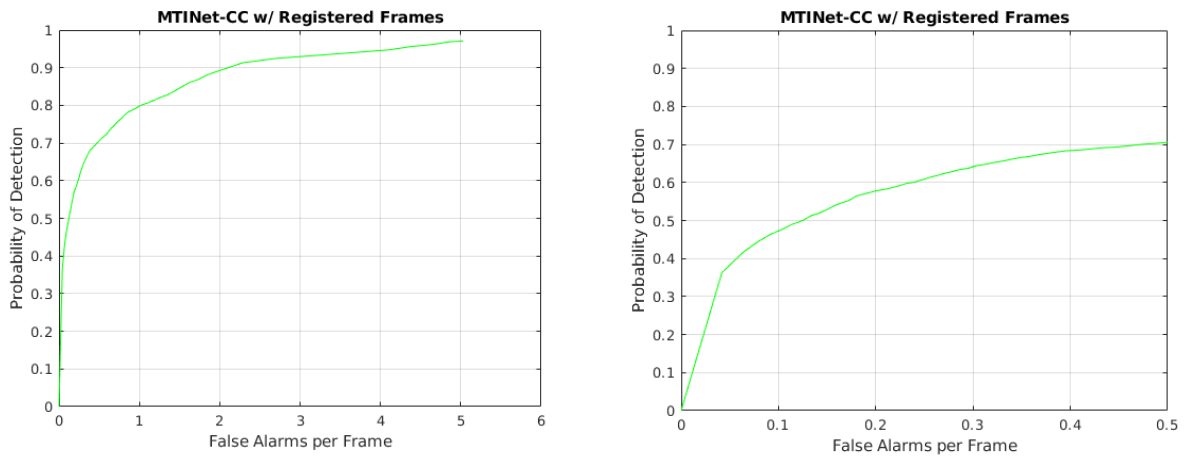

Figure 25: MTINet-CC results on NVESD testing set with registered frames

We can see that the registration of frames helps recover the overall performance of the network. The maximum probability of detection increases significantly from less than 30% back to approximately 98%. Figure 26 below compares the ROC curves between MTINet-CC results on the NVESD testing data without simulated sensor movement, MTINet-CC with misaligned frames, and MTINet-CC with registered frames.

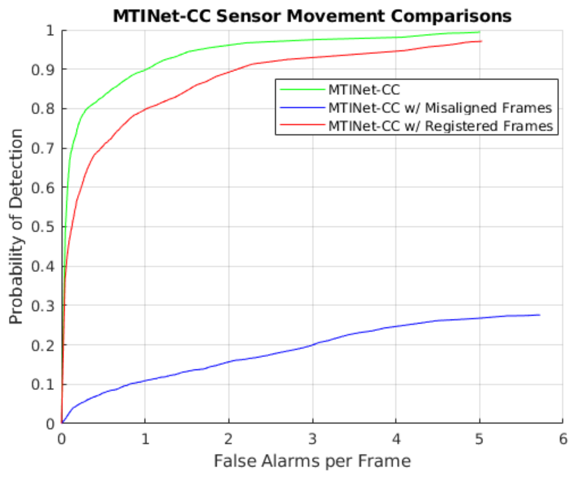

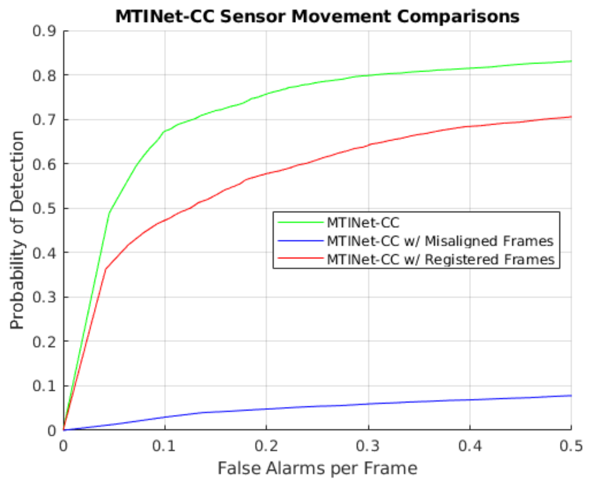

Figure 26: MTINet-CC results on NVESD testing set with and without sensor movement

Performance Evaluation of MTINet-DW

The performance of MTINet-CC on the NVESD testing data with simulated sensor movement reveals the shortcoming of this network architecture. Specifically, in Figure 26 we see that this architecture relies on the cross-dependencies for exploiting temporal information across each frame; however, the explicit connections made between each frame can be limiting to the network's performance. To ensure the explicit connections are not hindering the networks performance, we MTINet-DW architecture uses grouped convolutions for processing the frames independently rather than separate processing streams. Figure 27 below shows the results of MTINet-DW, on the NVESD testing data with registration to align the frames affected by sensor movement. The change in architecture helps push the probability of detection higher at the lower false alarm regions; however, the maximum probability of detection drops from 98% to 95%. At a false alarm rate of 0.5, the network achieves a probability of detection of approximately 74% whereas the prior architecture reached 70%.

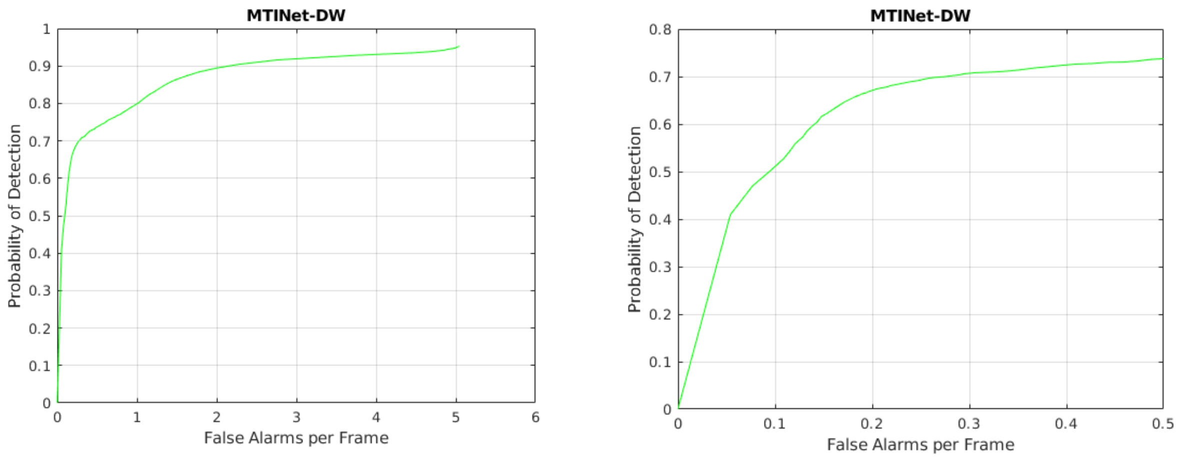

Figure 27: MTINet-DW results on NVESD testing data with registered frames

We further investigate the networks ability to localize a moving target using guided backpropagation to draw a heatmap of the activations produced by the last convolutional layer. Using the same process described in Experiment Analysis, we generate a heatmap using a block of five frames from the testing set. Figure 28 below shows the generated heatmap overlayed on the middle frame from the block of five frames. The heatmap shows that the network is able to accurately localize the target while producing almost no response to the surrounding clutter.

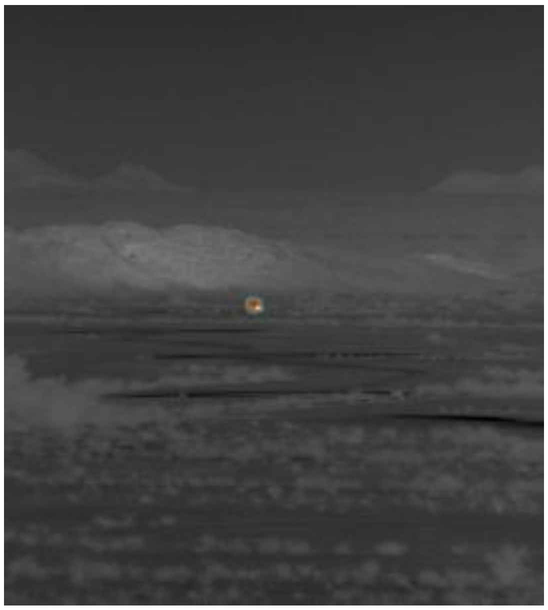

Figure 28: Activation Map of trained MTINet-DW

Evaluation of the ARX Algorithm

We compare the performance of the CNN approaches with the Reed-Xiaoli algorithm, repurposed for temporal change detection. This detector is most optimal when the temporal variations of the background pixels fits a gaussian distribution while the anomalies do not. Therefore, the intensity fluctuations at any given pixel due to noise is assumed to be gaussian, but not the variations that occur due to the movement of the target. Figure 29 below shows the results of ARX algorithm on the NVESD testing data with registered frames. The ARX algorithm reaches a maximum probability of detection of approximately 85% which is lower than that of the MTINet. However, the probability of detection at the lower false alarm ranges outperforms the MTINet. At a false alarm rate of 0.5, the ARX algorithm achieves a similar performance to MTINet-DW with a probability of detection of about 75%. However, at a false alarm rate of 0.1, the algorithm reaches a probability of detection of 60% which is higher than both MTINet-CC and MTINet-DW by about 10%.

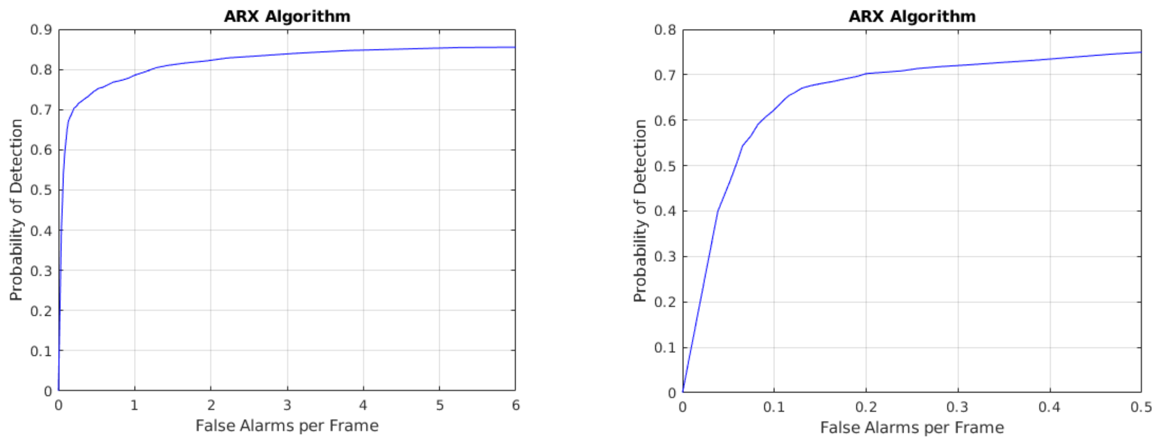

Figure 29: ARX Algorithm results on NVESD testing data with registered frames

<u>Combining MTINet and the ARX Algorithm</u>

Based on the results in Evaluation of the ARX Algorithm, we observed that the trained CNN's are better at finding more targets at higher false alarm rates but the ARX detector can find more targets at a lower false alarm rate. Therefore, we utilize the ARX algorithm concurrently with the MTINet-DW to combine the best of both approaches, i.e. the ability of the ARX algorithm to find more targets at low FAR with the ability of the MTINet-DW to find more targets overall. We do so by normalizing and merging the output detections then identifying likely accurate detections versus false alarms using the normalized confidence scores. Figure 30 below shows the effectiveness in combining the two algorithms on the NVESD testing data with registered frames.

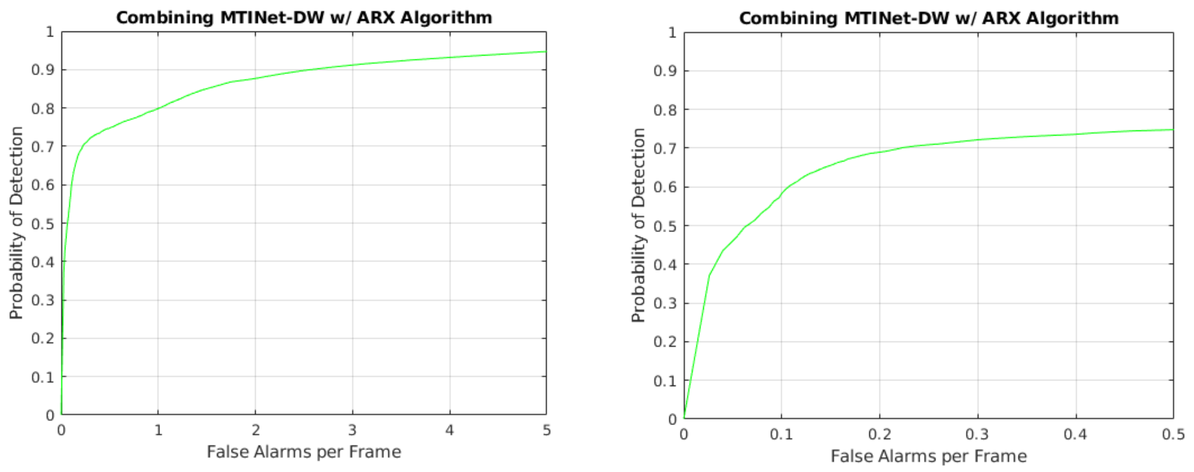

Figure 30: Combined MTINet-DW and ARX algorithm results on the NVESD testing data with registered frames

Figure 31 below compares the ROC curves of the combined algorithms versus the individual performance of each on the NVESD testing set with registered frames. We see that the combination bridges the gap between the 0 to 0.5 false alarm rate range and then continues to perform similarly to MTINet-DW above that range.

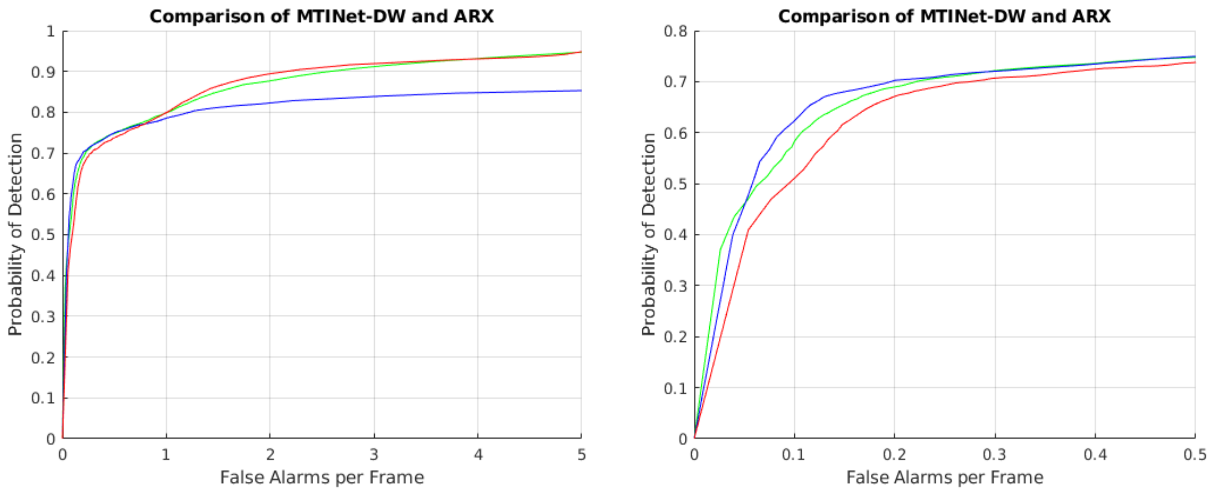

Figure 31: Comparison of MTINet-DW, the ARX algorithm, and their combination on the NVESD testing set

CHAPTER FIVE: CONCLUSION AND FUTURE WORK

In comparison to experiments done using state-of-the-art networks, the algorithms proposed here outperform the ability to detect small moving targets in the NVESD dataset. Using the highest performing variants of each experiment, we can see in Table 3 that MTINet-CC, MTINet-DW, and the combination of MTINet-DW and the Reed-Xiaoli algorithm all exceed results of the state-of-the-art networks. YOLOv3 achieves the lowest false alarm rate at its respective maximum probability of detection; however, that probability of detection is merely 32%. On the original NVESD testing data, MTINet-CC can detect every target but with a high false alarm rate. At a 0.1 false alarm rate, MTINet-CC is still able to detect approximately 68% of targets. The performance of MTINet-CC versus the state-of-the-art networks on the testing set is nearly 50% greater. This performance increase can likely be attributed to the additional exploitation of temporal information and an architecture that is built to incorporate that information. We also believe the modified TCR cost function helps guide our networks to discern target versus clutter.

Table 3: Comparing results of highest performance experiments

Network	Maximum PDet	FAR @ Maximum PDet	PDet @ 0.1 FAR	PDet @ 0.5 FAR
YOLOv3	0.32	**0.85**	0.15	0.27
Mask R-CNN	0.11	1.78	0.03	0.07
MTINet-CC*	**0.99**	5.0	**0.68**	**0.82**
MTINet-CC	0.97	5.0	0.47	0.70
MTINet-DW	0.95	5.0	0.51	0.73
MTINet-DW + ARX	0.95	5.0	0.59	0.75

** Results of MTINet-CC with no sensor movement*

When applying simulated sensor movement, we see a major drop in the detection ability; however, after introducing registration using SURF we're able to recover that performance. Figure 32 below shows the performance of MTINet-CC on the unaltered NVESD testing dataset in comparison with the results of other algorithms with simulated sensor movement. When introducing simulated sensor movement and registering the frames, each algorithm can reach closer to the performance on unaltered data. Notably, the ARX algorithm (which unlike CNN's, requires no training) also achieved reasonable results on the testing data. This makes the algorithm quickly deployable into real-time systems. Therefore, continuing to improve the performance of this algorithm for small moving target detection is worth pursuing.

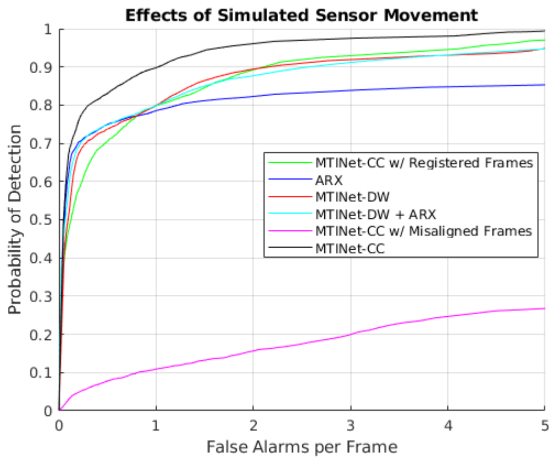

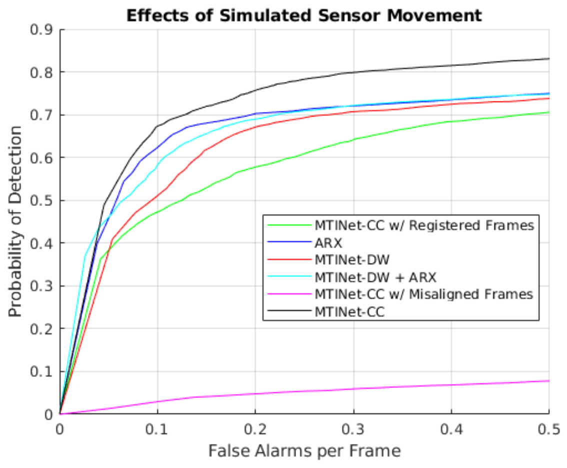

Figure 32: Comparison of results given simulated sensor movement

Although our algorithms perform well on the NVESD testing set compared to previous state of the art detectors, we will strive to reduce false alarm rates by an order of magnitude while further increasing probability of detection. We also believe there is a need to develop theoretical performance prediction techniques that can provide meaningful upper bounds on the performance that can be achieved on a particular data set. Furthermore, the performance of the MTINet must be optimized and evaluated under more challenging environmental conditions such as smoke, dust, and scintillations produced by atmospheric turbulence. Beyond, such effects observed in infra-red imagery, our ultimate goal is to create a network that can generalize to any type of imagery and accurately detect both stationary and moving objects that are small, medium, or large. We also aim to further develop the idea of the combination of multiple detection algorithms for optimal performance.

REFERENCES

[1] J. Redmon and A. Farhadi, "YOLOv3: An Incremental Improvement," 2018.

[2] K. He, G. Gkioxari, P. Dollár and R. B. Girshick, "Mask R-CNN," *CoRR,* vol. abs/1703.06870, 2017.

[3] I. S. Reed and X. Yu, "Adaptive multiple-band CFAR detection of an optical pattern with unknown spectral distribution," *IEEE Transactions on Acoustics, Speech, and Signal Processing,* vol. 38, no. 10, pp. 1760-1770, 1990.

[4] O. Russakovsky, J. Deng, H. Su, J. Krause, S. Satheesh, S. Ma, Z. Huang, A. Karpathy, A. Khosla, M. Bernstein, A. C. Berg and L. Fei-Fei, "ImageNet Large Scale Visual Recognition Challenge," *Springer,* vol. 115, no. 2015, pp. 211-252, 2015.

[5] T.-Y. Lin, M. Maire, S. Belongie, L. Bourdev, R. Girshick, J. Hays, P. Perona, D. Ramanan, C. L. Zitnick and P. Dollár, "Microsoft COCO: Common Objects in Context," *Springer,* vol. 8693, no. 2014, pp. 740-755, 2014.

[6] "ATR Algorithm Development Data Set," DSIAC.

[7] M. Tan, R. Pang and Q. V. Le, "EfficientDet: Scalable and Efficient Object Detection," 2020.

[8] S. Qiao, L.-C. Chen and A. Yuille, "DetectoRS: Detecting Objects with Recursive Feature Pyramid and Switchable Atrous Convolution," 2020.

[9] Z. Huang and J. Wang, "DC-SPP-YOLO: Dense Connection and Spatial Pyramid Pooling Based YOLO for Object Detection," *Information Sciences,* vol. 522, 2020.

[10] H. Zhang, C. Wu, Z. Zhang, Y. Zhu, Z. Zhang, H. Lin, Y. Sun, T. He, J. Muller, R. Manmatha, M. Li and A. Smola, "ResNeSt: Split-Attention Networks," *arXiv preprint,* 2020.

[11] C.-I. Chang and C. Shao-Shan, "Anomaly detection and classification for hyperspectral imagery," *IEEE Transactions on Geoscience and Remote Sensing,* vol. 40, no. 6, pp. 1314-1325, 2002.

[12] W. Sanghyun, J. Park, J.-Y. Lee and I. S. Kweon, "CBAM: Convolutional Block Attention Module," in *Computer Vision - ECCV 2018*, Springer International Publishing, 2018, pp. 3-19.

[13] J. Hu, L. Shen and G. Sun, "Squeeze-and-Excitation Networks," in *2018 IEEE/CVF Conference on Computer Vision and Pattern Recognition*, 2018, pp. 7132-7141.

[14] L. Kaiser, A. N. Gomez and F. Chollet, "Depthwise Separable Convolutions for Neural Machine Translation," *CoRR,* vol. abs/1706.03059, 2017.

[15] H. Bay, T. Tuytelaars and L. Van Gool, "SURF: Speeded Up Robust Features," in *Computer Vision -- ECCV 2006*, Springer Berlin Heidelberg, 2006, pp. 404-417.

[16] S. Hochreiter and J. Schmidhuber, "Long Short-term Memory," *Neural Computation,* vol. 9, pp. 1735-80, 1997.

[17] R. R. Selvaraju, A. Das, R. Vedantam, M. Cogswell, D. Parikh and D. Batra, "Grad-CAM: Why did you say that? Visual Explanations from Deep Networks," *CoRR,* vol. abs/1610.02391, 2016.

[18] J. Long, E. Shelhamer and T. Darrell, "Fully convolutional networks for semantic segmentation," in *2015 IEEE Conference on Computer Vision and Pattern Recognition (CVPR)*, IEEE, 2015, pp. 3431-3440.

[19] B. McIntosh, A. Mahalanobis and S. Venkataramanan, "Infrared Target Detection in Cluttered Environments by Maximization of a Target to Clutter Ratio (TCR) Metric using a Convolutional Neural Network," *IEEE Transactions on Aerospace and Electronic Systems,* pp. 1-1, 2020.

[20] S. Woo, J. Park, J.-y. Lee and I. S. Kweon, "CBAM: Convolutional Block Attention Module," *CoRR,* vol. abs/1807.06521, 2018.

[21] V. Mnih, N. Heess, A. Graves and K. Kavukcuoglu, "Recurrent Models of Visual Attention," in *Advances in Neural Information Processing Systems 2*, Curran Associates, Inc, 2014, pp. 2204-2212.

[22] A. Bochkovskiy, C.-Y. Wang and H.-Y. M. Liao, "YOLOv4: Optimal Speed and Accuracy of Object Detection," 2020.